

POLITECNICO DI TORINO

Master Degree in Electronic Engineering



**Politecnico
di Torino**

Master Degree Thesis

**Laser frequency characterization for new
generation atomic clocks**

Supervisor

Prof. Giovanni A. Costanzo

Candidate

Gaspare Antona

Co-Supervisors

Dr. Filippo Levi

Dr. Claudio E. Calosso

Dr. Salvatore Micalizio

Dr. Michele Gozzelino

Academic Year 2020/2021

October 2021

Abstract

Precise timekeeping plays a key role not only in science but also in many technological sectors, including aerospace, global navigation satellite systems, defense, and telecommunication. Very often, only atomic-based frequency references provide the required stability and accuracy. At the same time, the clocks used in technological applications should satisfy precise specifications in terms of size, weight, and power consumption (SWaP). In this regard, vapor-cell clocks based on alkali-metal atoms pumped by a laser have recently received considerable attention, providing low SWaP joined to interesting frequency stability performances.

The spectral characteristics of these lasers directly affect the standard stability performance, both in the short and in the medium-long term. Indeed, laser noise is transferred to the atoms, through several physical phenomena like light shift, non-homogeneities inside the clock cell, and so on. It is then of paramount importance to investigate the laser spectral behavior, also because laser noise measurements are rarely found in the literature.

This thesis presents the frequency-noise characterization of the laser diode currently employed in a high-performing Rb vapor-cell frequency standard developed at INRIM. The latter employs the pulsed optically pumping scheme (POP) and nowadays represents the state of the art for vapor-cell clocks.

The laser noise is measured in the range from 1 Hz to 100 kHz, which is of interest for the atomic clock operation. The assessment of the frequency noise level will allow completing the clock stability budget. The influence of the current driver on the laser-diode frequency noise is also investigated. Moreover, the behavior of the laser stabilization system is analyzed by comparing two independent setups. An upper limit for the frequency stability is measured to be 30 kHz at 7×10^4 s, which corresponds to a frequency instability contribution of 10^{-15} for the POP clock.

Table of Contents

List of Tables	v
List of Figures	vi
1 Introduction	1
1.1 Vapor-cell Rb clocks	2
1.2 POP clocks	5
1.2.1 Physics package	7
1.2.2 Optics package	8
1.2.3 Electronics package	8
2 Noise and diode laser characteristics for atomic clocks	10
2.1 Oscillator characterization	10
2.2 Commercial available laser diodes	15
2.2.1 Semiconductor lasers	15
2.2.2 Frequency doubled telecom lasers	17
2.3 Noise measurement techniques	17
2.3.1 Delay line method	17
2.3.2 Beatnote method	18
3 Laser setup and beatnote generation	21
3.1 Fiber laser stabilization system	22
3.2 Beatnote setup	23
3.3 DFB stabilization system	25
4 DFB frequency noise measurement	28
4.1 Frequency/Voltage converter	28
4.1.1 Calibration	29
4.1.2 Characterization	32
4.2 Beatnote frequency noise	34
4.2.1 Effect of power-line on the frequency noise	37

4.3	DFB laser frequency noise measurement	37
4.4	Current driver contribution	38
4.4.1	LDC201CU driver	38
4.5	Contribution of the current generator to the frequency noise	40
4.5.1	Other current drivers	41
5	Laser frequency long-term stability	45
5.1	Beatnote frequency characterization	45
5.1.1	DFB different locking bandwidth	47
5.2	POP clock frequency stability	49
6	Conclusions	52
	Bibliography	54

List of Tables

4.1	f/V converter coefficients.	31
4.2	Analog Signal Generator Agilent E8257D noise.	33
4.3	LDC201CU noise at different frequencies.	40
4.4	Laserlabs noise at different frequencies.	42
4.5	LDC200 noise at different frequencies.	43
4.6	LDC201-INRIM noise at different frequencies.	43
5.1	Phase noise.	47
5.2	Different error signal slope.	48
5.3	POP clock frequency stability.	50

List of Figures

1.1	Rb atomic clock, Temex Neuchâtel Time S.A., 1995 in collection of the Le Locle museum in Switzerland.	3
1.2	Physics package of the NIST chip scale atomic clock with a volume of 1 cm ³	5
1.3	Symmetricom chip scale atomic clock.	5
1.4	Energy levels of ⁸⁷ Rb.	6
1.5	Timing sequence in the POP clock with optical detection of the clock transition. Numerical values refer to the experiments made at INRIM, taken from [5].	6
1.6	Physics package of the POP clock taken from [7].	7
1.7	Electronics package of the POP clock with the main components highlighted taken from [10].	9
2.1	Amplitude and phase noise taken from [39].	11
2.2	Polynomial law of phase noise from [40].	13
2.3	Fractional frequency [40].	14
2.4	Allan variance AVAR [40].	14
2.5	DFB laser diode different packages. On the left there is the DFB SN FB-04038 used in the thesis work.	16
2.6	Scheme of the delay line (Homodyne) technique.	18
3.1	Koheras ADJUSTIK K822 NKT Photonics.	22
3.2	Fiber laser stabilization setup.	22
3.3	Fiber laser spectroscopy setup.	23
3.4	Optical circuit.	24
3.5	Frequency stabilization setup.	26
4.1	f/V converter scheme.	29
4.2	Frequency to voltage converter calibration.	30
4.3	Fitting and residue of -2 dBm curve.	31
4.4	f/V converter deviation from linearity.	32

4.5	f/V characterization scheme.	32
4.6	f/V noise floor with $P = +12$ dBm at different frequencies.	34
4.7	f/V noise floor with $\nu_c = 80$ MHz at different power values.	34
4.8	Beatnote measurement scheme.	35
4.9	SCAN error signal of ^{87}Rb energy levels.	36
4.10	Error signal with closed stabilized loop.	36
4.11	Beatnote noise at $\nu_c = 80$ MHz.	36
4.12	Beatnote noise at $\nu_c = 80$ MHz with different UPS.	37
4.13	Beatnote comparison between two different DFB.	38
4.14	LDC201CU monitor output with a voltage partition.	39
4.15	LDC201CU monitor output current noise.	39
4.16	Frequency noise of the beatnote and driver noise contribution.	41
4.17	Laser diode intrinsic frequency noise.	42
4.18	Laserlabs measurement scheme.	42
4.19	Noise comparison of current drivers. The left scale is referred to current noise in $\text{dB} \frac{\text{A}^2}{\text{Hz}}$, while the right to the frequency noise in $\text{dB} \frac{\text{Hz}^2}{\text{Hz}}$, obtained using the current-to-frequency coefficient in eq.(4.5).	43
5.1	Beatnote frequency characterization. A gate time of 26 ms for times < 2 s, while equal to 1.016 s when the time of measurements is longer.	46
5.2	Typical error signal in open-loop.	48
5.3	Comparison of the laser frequency stability.	49
5.4	Contribution of the laser to the POP clock frequency stability.	51

Chapter 1

Introduction

Currently, scientific experiments and many industrial applications, like the aerospace industry, global navigation satellite systems [1], defense and telecommunications [2] need very accurate time and frequency references [3, 4]. Compact atomic clocks presently guarantee the required high level of accuracy and stability. Laser-based vapor-cell clocks made of alkali-metal atoms are particularly suited for these applications [5], that demand good frequencies stability performances joined to compactness, reliability, and low power consumption [6].

The laser diode currently employed in a high-performing Rb vapor-cell frequency standard is developed at INRIM [7]. The pulsed optically pumping scheme (POP) is employed and nowadays represents the state of the art for vapor-cell clocks. This clock can be developed to export its performances for industrial applications, being attractive for the aerospace sector where precise timing is needed [8].

On the other hand, for this kind of application, it is essential to reduce size and weight because it implies better temperature control and compactness. For this reason, INRIM is involved in a technology transfer activity in support of Leonardo S.p.A. to create an engineered prototype of this clock suitable for space applications such as GNSS [9], under the supervisor of the European Space Agency [10].

The spectral characteristics of these lasers directly affect the standard stability performance, both in the short and in the medium-long term [11]. Indeed, laser noise is transferred to the atoms, through several physical phenomena like light-shift, non-homogeneities inside the clock cell, and so on. It is then important to investigate the laser spectral behavior, also because laser noise measurements are rarely found in the literature. Therefore, this thesis presents the frequency-noise characterization of the laser diode currently employed in the POP clock experiment developed at INRIM [7]. The thesis is organized as follows:

- in section 1.1 vapor-cell rubidium clocks are briefly reviewed. In particular the pulsed optically pumped clock is described;

- in chapter 2 the main laser technologies suitable for Rb clocks are reviewed, with an emphasis on the spectral characteristics;
- in chapter 3 the laser setup and stabilization systems are illustrated. Moreover, the beatnote setup used for the frequency noise characterization is described;
- in chapter 4 the frequency-to-voltage converter is characterized. The measurement setup is used to measure the frequency noise of different diode lasers. The effect of the laser current drivers is also discussed;
- in chapter 5 the laser frequency long-term stability and the impact on the POP clock are reported;
- in chapter 6 there are reported possible improvements such as new current drivers with lower frequency noise. Also, if the frequency analysis would be enlarged to more inputs can be obtained an absolute characterization of noise and stability.

1.1 Vapor-cell Rb clocks

Modern systems ranging from cell-phone communications to satellite navigation, defense and aerospace take advantage of atomic clocks, in particular of compact, reliable, and low-power Rb vapor-cell clocks [12].

Rubidium atomic clocks are used in modern GNSS [8], and the RF-discharge lamps play a primary role in the Rb clock's atomic signal generation and in modern timekeeping [13]. An example of such devices is reported in figure 1.1.

Progress has been made in recent years especially in digital electronics [14]. The discharge lamp produces light resonant with the Rubidium atomic transition. The light passes through a vapor of Rb atoms placed in a glass cell and it is detected by a photodiode. The light and the microwave generate the double resonance, because it is necessary to have a reference for the stabilized condition. The microwave synthesis is made from a quartz at low frequencies and the frequency is the output of the clock. Therefore, it is generated a train of one-second pulses for timekeeping. The lamplight is necessary for the optical pumping, which creates the necessary population imbalance between the atoms ground state hyperfine levels. The discharge lamp does not only drives the pumping effect, but also provides a signal that indicates if the microwave field is on resonance. Unfortunately, due to the light-shift effect, the lamplight in the resonance cell perturbs the Rb's energy level structure, producing a shifting of the clock levels [15]. Thus, instabilities of the lamp limit the medium- and long-term stability of the vapor cell [16].

The rubidium atomic frequency standard (RAFS) was the first frequency standard to be tested in a suborbital flight in 1961 [14]. It is the first having been sent

into deep space for the Cassini-Huygens mission in 1977. The two units sent were necessary to achieve sufficiently stable communication between the receiver and the transmitter during the Doppler wind experiment descent time [17, 18].

Rubidium clocks aboard satellites operate under different conditions than do terrestrial clocks, and they need to adapt to those conditions has led to a range of physical and chemical research. The glass surface of a discharge lamp is hit by energetic ions etching the surface and alkali-metal atoms interacting with the exposed glass [19].



Figure 1.1: Rb atomic clock, Temex Neuchâtel Time S.A., 1995 in collection of the Le Locle museum in Switzerland.

The problem of Rb lamps are short lifetime and reliability, so after different researches, the development of single-mode semiconductor laser diodes in the 1980's opened new interesting prospects in the gas cell frequency standards thanks to the possibility of replacing the discharge lamp with a laser source resonant on D1 or D2 spectral lines of alkali-metal atoms [20].

Laser-pumped vapor-cell clocks have been actively investigated, to improve the control of the light-shift effect, the optical pumping, and the clock frequency stability, and providing compactness, reliable and low power consumption [5].

At first, the continuous-wave (CW) double-resonance (DR) Rb clock with laser optical pumping is used, where a laser diode is tuned to D2 optical transition of ^{87}Rb replaces the lamp as a source. The laser is frequency locked to the optical line using an external cell containing only ^{87}Rb by the common sub-Doppler saturated absorption technique [21]. The single-mode diode laser makes a more efficient pumping, a larger signal, and a higher signal-to-noise ratio. With the CW configuration, the light-shift can be mitigated but it is still present, limiting the performances of laser-pumped DR clocks [22]. Moreover, coherent transfer of frequency and intensity noises of the laser can impact the short-term stability [11].

Therefore, different laser sources are used in the years to investigate the continuous laser optical pumping technique of rubidium atomic frequency standard (RAFS) [23].

The lasers are often used because of narrow spectrum, rather than for coherence. Instead, an important phenomenon in which the coherence properties are fully exploited is coherent population trapping (CPT), an alternative interrogation method that has been successfully used to implement Rb vapor-cell [24]. The CPT technique is based on two phase-coherent lasers, when the difference in frequency between the two intensities is equal, the light-shift effect disappears. But this is only a first-order cancellation of light-shift, and a reduction of the laser noise problems [5]. For its implementation the laser is modulated at one-half the atomic hyperfine frequency to excite the atoms in a gas cell to produce sidebands in the spectrum above and below the unperturbed laser frequency, eliminating the need for a microwave cavity [25].

CPT atomic clocks became very diffused because allow a strong reduction in size to have chip-scale devices. The chip-scale atomic clock (CSAC) offers a significantly smaller size, lower power consumption, and lower cost than a traditional atomic clock with a reduction of an order of magnitude of short-term frequency stability [26, 27]. The physics package of the National Institute of Standards and Technology (NIST) chip-scale atomic clock is reported in figure 1.2, which includes a laser, a lens, an optical attenuator to reduce the laser power, a waveplate that changes the polarization of the light, a cell containing a vapor of cesium atoms, and a photodiode to detect the laser light transmitted through the cell. The tiny gold wires provide electrical connections to the electronics for the clock.

The commercial frequency references CSAC have physics packages near 1 cm^3 in size, total power dissipation less than 1 W and they are very low cost, about few hundred dollars, like the one made by Symmetricom in figure 1.3. For measurement of about one day, their long-term frequency instability is below 10^{-11} .

These devices are developed with the Defense Advanced Research Projects Agency (DARPA) [28] and they are used in different commercial applications, such as the defence, global navigation satellite systems receiver [8, 29], and telecommunications [30]. But CSAC suffers from internal systematic instabilities and errors that should be minimized if optimal performance is desired.

If the pump-probe light is switched off during the clock interrogation phase, light-shift is greatly reduced. This is the main motivation towards the development of a device working in a pulsed regime. Therefore, researchers decided to move into the pulsed optical pumped (POP) clocks to resolve the CPT and CSAC problems. In the traditional technique, the atoms pass through the microwave cavity twice, with a free-space evolution in the middle.

In the POP clock, the Ramsey technique is used to realize the clock interrogation

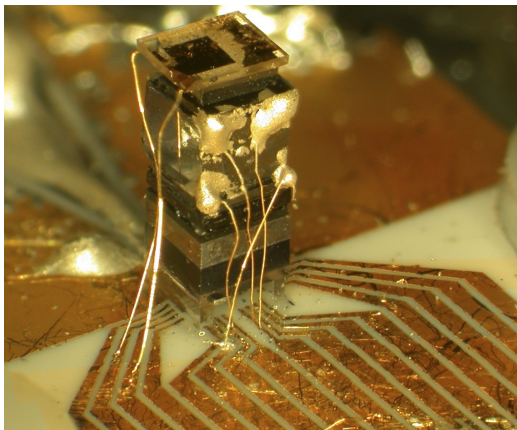


Figure 1.2: Physics package of the NIST chip scale atomic clock with a volume of 1 cm^3 .



Figure 1.3: Symmetricom chip scale atomic clock.

[31]. Two phase-coherent microwave pulses are sent to the microwave cavity, separated by a free-evolution time, while the atomic motion is constrained by the presence of a buffer gas. The atoms interact with a pump laser pulse, then with the microwave as the laser is turned off (dark time). Finally, the laser is used as a probe only to discover how many atoms performed the clock transition. In recent years the team led by A. Godone at INRIM realized a laser pulsed optically pumped standard, with microwave detection and then with optical detection [7, 32].

In the following paragraph 1.2, the fundamental characteristic of the latest prototype will be resumed.

1.2 POP clocks

This section resumes the main characteristics of the POP clock developed at INRIM [7]. The latest prototype uses a laser resonant with the Rb D_2 line ($F = 2 \rightarrow F' = 2,3$ transition); figure 1.4 depicts the energy levels of the clock transition and of the pumping and detection transitions.

The POP clock operation is based on the time separation of three different phases: preparation, interrogation, and detection [31], as reported in figure 1.5. The atomic sample is prepared by a laser pulse producing a population imbalance between the two ground-state hyperfine levels of ^{87}Rb . The atoms are then interrogated with a couple of microwave pulses resonant with the clock transition (6.834 GHz) and separated by a time T (Ramsey interaction). At last, the atoms that have done the transition are detected during the detection phase. This technique makes a

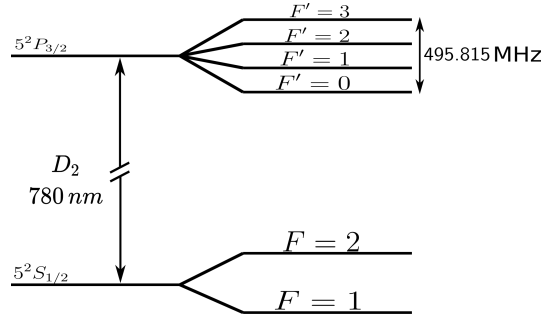


Figure 1.4: Energy levels of ^{87}Rb .

reduction of the light-shift compared to both the DR approach [33] and the CPT technique [34] because the atoms make the clock transition when the laser is turned off. Furthermore, the Ramsey interrogation technique allows one to observe a clock signal with a narrow linewidth that is mostly insensitive to any working parameter.

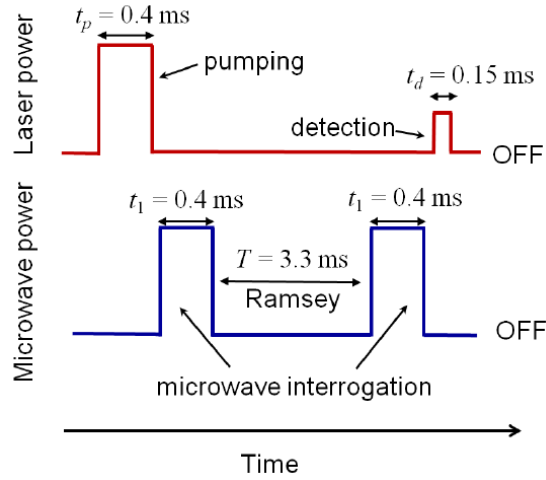


Figure 1.5: Timing sequence in the POP clock with optical detection of the clock transition. Numerical values refer to the experiments made at INRIM, taken from [5].

The POP clock setup is divided into three blocks: physics, optics and electronics packages (resumed in sections: 1.2.1, 1.2.2 and 1.2.3 respectively) [7, 10].

1.2.1 Physics package

The physics package (sketched in figure 1.6) includes the cavity-cell, the quantization field solenoid, thermal and magnetic shields to set and stabilize the operational working points. It has a layered structure, where the core of the atomic clock is a quartz (fused silica) cylindrical cell with a radius equal to 1 cm and length of 2 cm, containing the atomic sample.

The cell also contains a mixture of buffer gases, argon Ar and nitrogen N_2 , in the ratio of 1.6 with a total pressure of 25 torr. The mixture of gas is at 65°C to minimize the temperature sensitivity [35]. The cell is placed in a cylindrical microwave cavity tuned near the 6.834 GHz Rb ground-state hyperfine transition frequency and resonates on the electromagnetic mode TE_{011} .

The microwave cavity has an internal diameter of 5.2 cm and length of 4.9 cm and is used to excite the magnetic dipole transition between the two clock states. It is made of molybdenum, a metal with good electric conductivity and a low thermal expansion coefficient. The cell-cavity volume ratio is optimized for ensuring the best trade-off between a good uniformity of the microwave field at the center of the cavity and a large volume of interacting atoms.

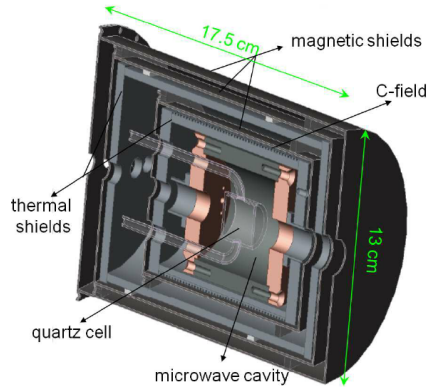


Figure 1.6: Physics package of the POP clock taken from [7].

The cavity is placed inside an aluminum cylinder which acts as an oven to bring the cavity and the clock cell at the operational temperature. This cylinder contains a solenoid that provides the quantization magnetic field. The cylinder is placed inside a magnetic shield, which is contained in a second aluminum cylinder supporting the external heater. The latter serves as a thermal shield and its temperature is stabilized [35].

Other two layers of magnetic shielding complete the package. All the physics package is placed under vacuum at 2×10^{-7} mbar, in a dedicated vacuum chamber. Thermal insulation is ensured and barometric effects due to ambient pressure and

humidity changes are prevented [36, 37].

1.2.2 Optics package

The optics package includes the laser head, which is a distributed-feedback laser (DFB) from Eagleyard, with a linewidth of about 2 MHz. The diode delivers about 25 mW of optical power to the experiment when driven with 100 mA [7]. An isolator prevents optical feedback from spurious reflections. Few optics, in particular a half-waveplate followed by a polarizing beam-splitter (BS), addresses part of the power to the stabilization of the laser frequency on an external reference cell containing isotopically enriched ^{87}Rb .

The main part of the laser beam is sent to the physics package through a single-pass AOM, that acts as an optical switch with at least 40 dB of attenuation for the pulsed operation.

This thesis will treat the Eagleyard laser diode in terms of noise and stability.

1.2.3 Electronics package

The electronics provides the signal acquisition chain as well as the pattern generator which sets the timescale of all the clock signals. The computational core of the electronics part is a field-programmable gate array (FPGA), which processes the input signals and manages the frequency loop. The correct impedance and signals dynamic range are obtained with a set of analog-to-digital converters (ADCs) and a signal conditioning unit (SC) in input, whereas at the output there is a set of digital-to-analog converters (DACs). The FPGA can run different general-purpose loop functions, used for the main frequency loop of the clock or to additional locking schemes.

The electronics board also includes the microwave synthesis chain, described in detail in [38].

The latter is made from a commercial unit (Pascall XMN) composed of a 100 MHz oven-controlled crystal oscillator (OCXO) and a direct multiplication stage which delivers a low-phase-noise output at 1.6 GHz, whereas a Direct Digital Synthesizer (DDS) generate a baseband signal at 34.7 MHz that is upconverted twice to reach the atomic clock frequency, 6.834 GHz, required by the Ramsey interaction scheme. The board is shown in figure 1.7 and includes another DDS that produces the 80 MHz radiation necessary to drive the single-pass AOM.

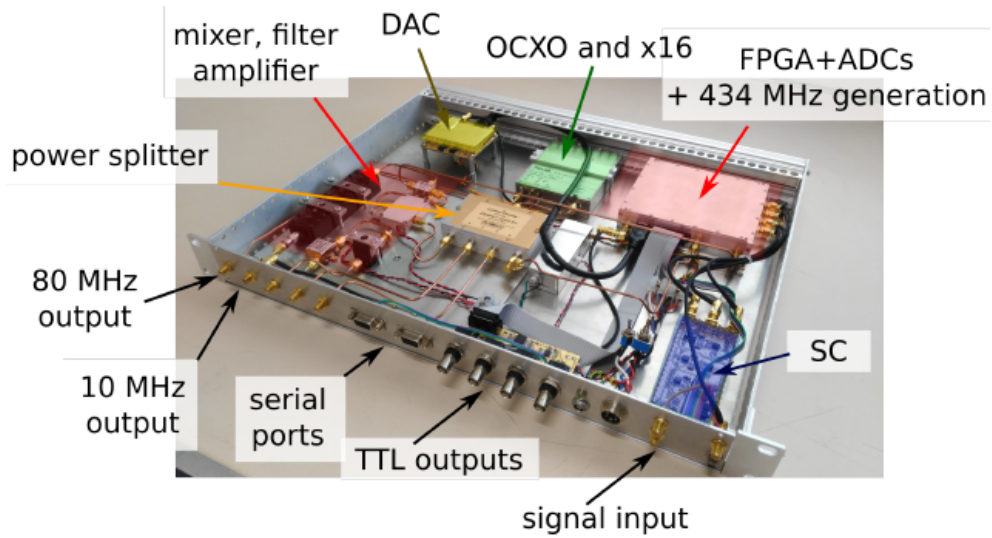


Figure 1.7: Electronics package of the POP clock with the main components highlighted taken from [10].

At last, a transimpedance amplifier with low input-current noise, Analog device AD8671, with a conversion factor of 1.6×10^4 V/A is used to detect the light transmitted through the cell during the detection stage.

Chapter 2

Noise and diode laser characteristics for atomic clocks

2.1 Oscillator characterization

An oscillator is a physical object that oscillates sinusoidally for a long time without losing its energy. In digital electronics, the oscillator that sets the timing of a system is also referred to as the clock. Atomic clocks are oscillators used for timekeeping, so it is important to know their characteristic noise. The oscillator can be characterized in the time domain for long time and in frequency domain for short measurements. The spectrum is used in frequency domain, whereas the Allan variance for the time one. Analyzing a signal, all the power is concentrated on the oscillator frequency, but some sidebands are produced on both its sides, due to phase, frequency and amplitude fluctuations.

Clock signal An oscillator signal fluctuates both in amplitude and phase; it can be modelled as [39]:

$$v(t) = V_0[1 + \alpha(t)] \cos[\omega_0 t + \varphi(t)] \quad (2.1)$$

where V_0 is the peak amplitude, $\alpha(t)$ is the random fractional amplitude, that must be $|\alpha(t)| \ll 1$, $\varphi(t)$ is the random phase, (also $|\varphi(t)| \ll 1$). Both amplitude (AM) and phase noises (PM) are present in all real signals, as shown in figure 2.1. Phase noise $\varphi(t)$ can be described as the time fluctuations, $x(t) = \frac{\varphi(t)}{2\pi\nu_0}$. The quantity $x(t)$ is independent on the carrier frequency and it can be used to compare different oscillators.

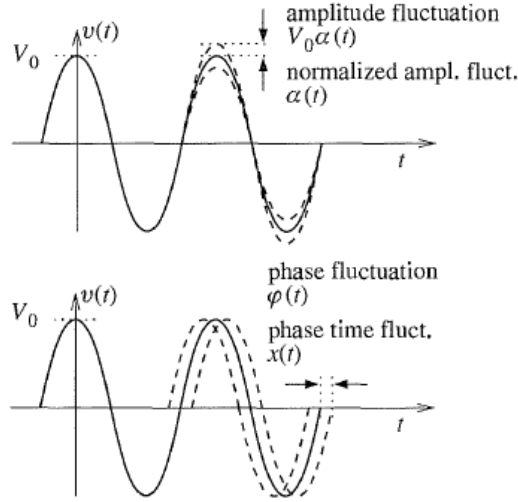


Figure 2.1: Amplitude and phase noise taken from [39].

The oscillator can be characterized in terms of frequency noise. Random frequency fluctuations are the time derivative of the phase fluctuations:

$$\Delta\nu_0(t) = \frac{1}{2\pi} \cdot \frac{d\varphi(t)}{dt} \quad (2.2)$$

where the quantity $(\Delta\nu_0)$ is the random frequency fluctuation, expressed in Hz. Also, the fractional frequency fluctuation $y(t) = \frac{d\varphi(t)}{2\pi\nu_0 dt}$ is derived, doing the normalization respect ν_0 of the instantaneous one.

The oscillator noise randomness is attributed to the frequency noise [39]. The frequency fluctuation associated with a phase fluctuation is derived by the equation 2.2. So, the white frequency noise, or white FM noise, is a parametric process originated by white noise which modulates the frequency of an oscillator. The phase noise power spectral density (PSD) associated with a white FM noise process is proportional to $1/f^2$. The flicker frequency noise, or flicker FM noise, has a PSD proportional to $1/f^3$ and finally the random walk of frequency proportional to $1/f^4$.

Power Spectral Density (PSD) The power spectral density of the signal describes the power present in the signal as a function of frequency, per unit of frequency, with physical dimension W/Hz. But, the signal can be also defined in terms of voltage, current, or phase, so, the power is simply estimated in terms of the square of the signal, always proportional to the actual power delivered by that signal. Thus, the PSD of the voltage $S_V(f)$, current $S_A(f)$ and phase $S_\varphi(f)$ have respectively physical dimensions of V^2/Hz , A^2/Hz and rad^2/Hz .

Generally, the one sided power spectral density $S_x(f)$ associated to the random process $x(t)$ can be defined as a distribution. A power spectral density is the measure of signal power content versus frequency. It is the quantity of power for each frequency component: therefore, PSD integral (in frequency domain) is the total signal power. For continuous signals over all time, the power spectral density exists for stationary processes. The power can be the actual physical power, or for convenience with abstract signals, is simply identified with the squared value of the signal. The average power of a signal $x(t)$ over all time is therefore given by the following time average, where the period T is centered about some arbitrary time $t = t_0$:

$$P = \lim_{T \rightarrow \infty} \frac{1}{T} \int_{t_0-T/2}^{t_0+T/2} |x(t)|^2 dt \quad (2.3)$$

Analyzing the frequency content of the signal $x(t)$, it is possible to compute the Fourier transform $\hat{x}(f)$, and the PSD as its integrand.

$$PSD = \lim_{T \rightarrow \infty} \frac{1}{T} |\hat{x}(f)|^2 \quad (2.4)$$

The power spectral density is measured with the FFT spectrum analyzer (SA).

Phase Noise in frequency domain Phase noise in oscillators can be described as a sum of polinomials, in eq.(2.5):

$$S_\varphi(f) = \sum_{n \geq -4}^0 b_n f^n \quad (2.5)$$

where the coefficients b_n are the parameters that describe the corresponding noise process. Phase noise spectra are plotted on a log-log scale. This is underlined in figure 2.2, where the various terms can be find, f^0 that is constant, $1/f$, $1/f^2$ and so on.

The additive noise can be decomposed in *white* phase and amplitude noise. The *flicker PM* is a parametric noise proportional to $1/f$.

Frequency noise in frequency domain Using the Fourier transform properties, the time domain derivative maps into a multiplication of ω^2 in the spectrum. So, eq.(2.6) is obtained to convert the phase noise spectrum into the frequency one.

$$S_{\Delta\nu}(f) = f^2 S_\varphi(f) \quad (2.6)$$

Thus, recalling the fractional frequency fluctuation $y(t) = \frac{d\varphi(t)}{2\pi\nu_0 dt}$, the PSD of eq.(2.6) becomes:

$$S_y(f) = \frac{f^2}{\nu_0^2} S_\varphi(f) \quad (2.7)$$

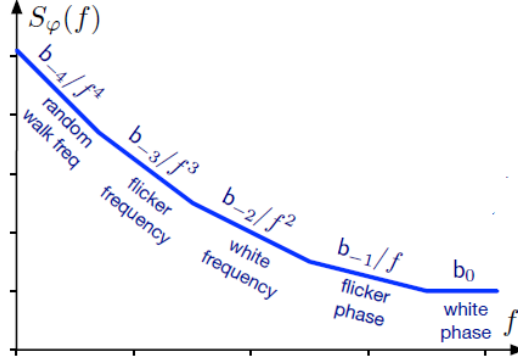


Figure 2.2: Polynomial law of phase noise from [40].

Applying the polynomial law on the eq.(2.7), the following equation is deduced (2.8):

$$S_y(f) = \sum_{n=-2}^2 h_n f^n \quad (2.8)$$

Therefore, in the frequency domain it is possible to refer, *random walk*, *flicker*, *white* noise and *flicker* phase noise ($n=1$) and *white* phase noise ($n=2$), which describe the slope of spectral density in a log-log scale [41].

Amplitude noise Another important noise contribution is the amplitude noise [42]. *White* noise (f^0) and *flicker* noise ($1/f$) are the dominant contributions.

AVAR As an alternative to spectral analysis the frequency stability can be evaluated in time domain. It is given a discrete set of time deviations x_i taken in sequence for the measurable time difference between a pair of clocks or between a clock and some primary reference. And also given the nominal spacing between adjacent time difference measurements τ_0 , the average fractional frequency for the i_{th} measurement interval is:

$$\bar{y}_i^{\tau_0} = \frac{x_{i+1} - x_i}{\tau_0}. \quad (2.9)$$

where $\bar{y}_i^{\tau_0}$ denotes the average over an interval τ_0 . A set of discrete frequency values can be constructed from a time-difference data set.

The Allan variance or AVAR is used as a standard for the time domain characterization of the oscillator [43]. Two sample variance:

$$AVAR = \langle \sigma_y^2(\tau) \rangle = \frac{1}{2} [\bar{y}_{k+1} - \bar{y}_k]^2 \quad (2.10)$$

where \bar{y}_k is the average fractional frequency, assuming that the two samples are contiguous in time, whereas the deviation is the square root of variance:

$$ADEV = \sigma_y(\tau) = \sqrt{\sigma_y^2(\tau)} = \sqrt{AVAR} \quad (2.11)$$

Both the PSD of frequency noise and the two-sample variances are valid measurements of the frequency stability. In frequency domain the Allan variance is equivalent to a filter with transfer function $|H_A(f)|^2$. Knowing that for AVAR, $|H_A(f)|^2 = 2 \frac{\sin^4(\pi\tau f)}{(\pi\tau f)^2}$, eq.(2.11) becomes:

$$\sigma_y^2(\tau) = \int_0^\infty S_y(f) |H_A(f)|^2 df \quad (2.12)$$

with $\int_0^\infty |H_A(f)|^2 = \frac{1}{2\tau}$, therefore the filter response to white noise $S_y(f) = h_0$ is $\sigma_y^2(\tau) = \frac{h_0}{2\tau}$.

Relationship between spectra and Allan variance The relationship between the $S_\varphi(f)$ and $S_y(f)$ is exact, so it is possible to convert these without loss of information, as reported in figure 2.3. The conversion from spectra to variance is shown in figure 2.4.

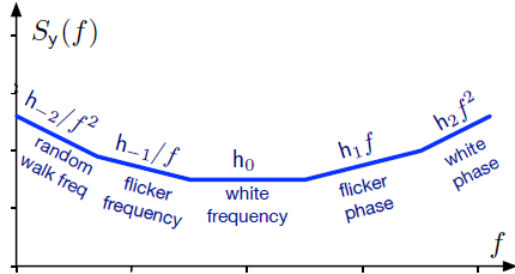


Figure 2.3: Fractional frequency [40].

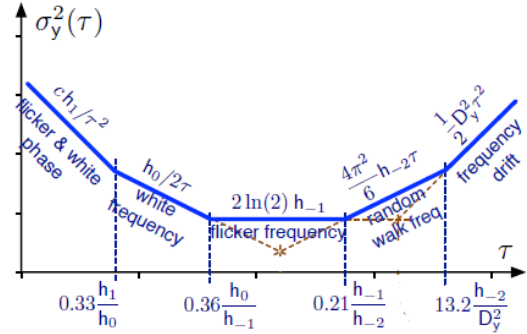


Figure 2.4: Allan variance AVAR [40].

Linewidth The laser linewidth is the full width at half-maximum (FWHM) of its optical spectrum. Precisely, it is the width of the power spectral density of the emitted electric field in terms of frequency and wavelength [44]. Using the root-mean-square (rms) value of the instantaneous optical frequency is defined:

$$\Delta\nu_{rms} = \sqrt{\int_{f_1}^{f_2} S_{\Delta\nu}(f) df} \quad (2.13)$$

The linewidth is calculated from the power spectral density $S_{\Delta\nu}(f)$ of the instantaneous frequency. Also, the noise frequencies can be evaluated between limited integration range [45].

The temporal coherence is related to the light beam linewidth. The finite latter arises from phase noise if the optical phase undergoes unbounded drifts. If drifts of the resonator are present, they could contribute to the linewidth and can make it dependent on the measurement time. On the other hand, the linewidth does not provide full information on the spectral purity of laser light, thus, more data are required for full noise specifications [44].

2.2 Commercial available laser diodes

The word laser is an acronym for light amplification by stimulated emission of radiation. In 1960 Theodor H. Maiman has realized the first solid state laser, using the stimulated emission phenomena [46]. Later, a gas laser was developed using a mixture of neon and helium [47]. Then, the GaAs semiconductor lasers operating at room temperature were realized [48] and improved in the successive years, creating the nowadays available laser diodes. Moreover, the fiber laser is developed to answer the raising demand for high-speed telecommunications due to the growth of the world wide web.

The most varied laser applications require lasers with a very small optical linewidth. The term narrow-linewidth lasers is usually applied to single-frequency lasers. In particular, the ones that oscillate on a single resonator mode have low phase and intensity noise and thus high spectral purity [49].

Diode with a small linewidth makes more efficient optical pumping which in turn enables to detect of the atomic resonance with enhanced contrast. For fixed resonance width and low noise levels, higher contrast turns into better short-term stability [50].

2.2.1 Semiconductor lasers

Semiconductor lasers are belonged to the category of solid-state lasers. Concerning to the latter, semiconductor lasers are more compact and efficient with the current injection phenomena instead of the excitation of the atoms. They are made by a p-n junction where electrons and holes recombine in a direct bandgap semiconductor in order to reach the lasing condition [44].

Different semiconductor lasers at 780 nm are described in the following paragraphs.

Distributed feedback laser diodes (DFB lasers) A distributed feedback laser is a single frequency laser diode. The resonator acts as a distributed Bragg

reflector in the wavelength range of laser action, so to stabilize the wavelength, a diffraction grating is etched close to the p-n junction. This grating acts as an optical filter, so provides the feedback required for lasing, thus reflection from the facets is not required. One facet of a DFB is anti-reflection coated. Typical operational characteristics are an output power of one hundred milliwatts and a linewidth of several megahertz [51]. In figure 2.5 there are reported different laser diodes packages.

Distributed Bragg reflector lasers (DBR lasers) A DBR laser resonator is made with at least one distributed Bragg reflector outside the gain medium. A DBR is a Bragg mirror, in some cases a quarter-wave mirror, providing the maximum amount of reflection for the given number of layers. Compared with a DFB laser, which consists of a single grating, a DBR laser has a longer laser resonator and thus higher output power, higher power efficiency, and narrower linewidth, typically a few megahertz [52]. Optics clocks are made by edge-emitting DBR, which have a square cavity and emit at one of the extremes.



Figure 2.5: DFB laser diode different packages. On the left there is the DFB SN FB-04038 used in the thesis work.

External-cavity diode lasers (ECDL) In the following years, the installation of wave division multiplexing systems will create a demand for tunable diode laser transmitters. Indeed, it is necessary to have lasers that emit at any desired wavelength, so in the late 1990s started the development of tunable diode lasers. The external cavity diode laser, with an adjustable mirror outside the semiconductor chip is used to select a particular wavelength [53]. Other types of external-cavity lasers use resonators based on optical fibers. Linewidth of a few kilohertz can be achieved by the latter.

ECDL are used for a greater coherence in the CPT laser and also for the narrower linewidth.

2.2.2 Frequency doubled telecom lasers

Fiber lasers rely on an optical fiber doped with different ions, such as erbium (Er^{3+}), neodymium (Nd^{3+}), ytterbium (Yb^{3+}) as the active gain medium. They could give light amplification without exploiting a resonant cavity. Most fiber lasers are optically pumped through semiconductor lasers, and suitable beam coupling devices are needed to inject the pumped radiation into the core [54].

The structure is a double-clad fiber, with a gain medium that forms the core of the fiber, which is surrounded by two layers of cladding. The lasing mode propagates inside the core, while a multimode pump beam propagates in the inner cladding layer. On the other hand, the outer cladding keeps light confined inside. This configuration allows a higher-power beam inside the core and the conversion of pump light with low brightness into a much higher-brightness signal [55].

Fiber lasers are mostly employed in telecommunication systems, material processing, defense, spectroscopy, medicine, and frequency stabilization systems [56]. The last one, in particular, is the use that it is made in this thesis. The fiber laser used is the low noise single-frequency Koheras ADJUSTIK K822 made by the NKT Photonics, which has a wavelength of 1560 nm.

Particularly, for Rb vapor-cell atomic clocks, the availability of lasers emitting at 780 nm presents a limitation for their commercialization. Therefore, the frequency-doubled fiber laser sources is used to Rb vapor-cell atomic clocks. Many companies have commercial devices based on different technologies diode and fiber lasers corresponding to the telecommunication C-band at 1560 nm, so reliable, low-cost optics components, and narrow linewidth are available. So, narrow telecom fiber lasers are needed and also absolutely stable in frequency and in time. Therefore, thanks to the second-harmonic generation (SHG) technology, 1560 nm different lasers can be duplicated at 780 nm to stabilize with the Rb cell and to have a long-term reference [57].

2.3 Noise measurement techniques

Different techniques to measure the frequency noise can be exploited, such as the delay line method 2.3.1 and the beatnote method 2.3.2.

2.3.1 Delay line method

The homodyne detection or delay line method has both waves always derived from the same laser source, reported in figure 2.6. This technique is an efficient approach for the measurement of the frequency fluctuations of frequency sources. Delay lines are used in optics to reach a signal uncorrelation for times less than the line delay

[58]. The red blocks represent the optic elements while after the photodiode the signal is analyzed with electronic blocks in yellow.

The laser light is split into two paths, one of which is delayed respect to the other before both beams are recombined, and the resulting response is measured with the FFT spectrum analyzer.

A variation is the self-heterodyne setup, where an acousto-optic modulator (AOM) is used to shift the beat note in frequency by w_m , in order to reject the detected DC signal in the photodiode and to allow use of a standard RF spectrum analyzer to measure the spectrum [59].

The two interfering fields have the same mean optical frequency. When the time delay τ_d of delay line in the interferometer is greater then the coherence time $\tau_{coherence}$, the mixed signals will be uncorrelated and the measured beatnote signal is not sensitive to the mean phase difference of the fields. But for correlated fields the observed homodyne spectrum becomes critically dependent on the optical phases [60]. The differential phase shift of the nominal frequency ν_0 caused by the delay line is obtained in eq.(2.14).

$$\Delta\phi = 2\pi\nu_0\tau_d \quad (2.14)$$

The phase fluctuations can be derived to the frequency fluctuation at the mixer. Therefore, using the formulas on the application note [61], the relationship between the two noise spectra is obtained, in eq.(2.15).

$$S_\varphi(f) = (2\pi\tau_d)^2 S_\nu(f) \quad (2.15)$$

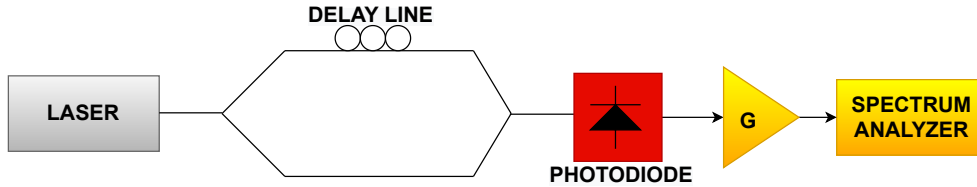


Figure 2.6: Scheme of the delay line (Homodyne) technique.

2.3.2 Beatnote method

Another technique to measure the frequency noise is the beatnote one. The beatnote is the difference in frequency between two laser sources using the heterodyne detection [58]. Two lasers at different frequencies are superimposed to measure the optical intensity and the noise behavior, so it is possible to observe the beatnote if some conditions are met [62]:

- the laser beams are overlapped and not orthogonal;
- the polarization must be not orthogonal;
- the beatnote optical frequency difference must be in the photodetector bandwidth;

The electromagnetic theory of light obeys the superposition principle, namely the electric field $E(t)$ on a single detection point, where the two beams are superimposed, can be written as the sum, in the case of the two harmonic sources:

$$E(t) = E_1 \cdot \cos(2\pi f_1 t) + E_2 \cdot \cos(2\pi f_2 t) \quad (2.16)$$

It is possible to assume that the two sinusoidal signals 1 and 2 are due to traveling waves, which are propagating collinearly. The frequencies of the two laser beams, f_1 and f_2 , are distinct and the polarization of E_1 and E_2 are perpendicular to the direction of propagation [63]. The superposition of the two signals produces the beatnote, a linear overlap of the fields. The two laser beams at the inputs of a beam splitter (BS), travel to the output where a photodetector is placed. This one reacts as the local energy density, which is proportional to the square of the electric field. So, for the electric field of eq. (2.16), this gives:

$$|E(t)|^2 = E_1^2 \cdot \cos^2(2\pi f_1 t) + E_2^2 \cdot \cos^2(2\pi f_2 t) + 2E_1 \cdot E_2 \cos(2\pi f_1 t) \cos(2\pi f_2 t), \quad (2.17)$$

which now exhibit the double product, in the case of waves superposition. Thus, trigonometric identities allow rewriting the eq. (2.17):

$$\begin{aligned} |E(t)|^2 = & \frac{1}{2} E_1^2 [1 + \cos(2\pi \cdot 2f_1 t)] + \frac{1}{2} E_2^2 [1 + \cos(2\pi \cdot 2f_2 t)] + \\ & + E_1 \cdot E_2 [\cos(2\pi(f_1 + f_2)t) + \cos(2\pi(f_1 - f_2)t)] \end{aligned} \quad (2.18)$$

The photodetector is unable to response to very high frequencies $2 \cdot f_1$, $2 \cdot f_2$ and $f_1 + f_2$ which are estimated in eq. (2.18), but it is fast enough to follow the frequency difference $f_1 - f_2$. For the two fields with the same polarization, the photodetector output is proportional to the time average of eq. (2.18), giving:

$$\langle |E(t)|^2 \rangle = \frac{1}{2} E_1^2 + \frac{1}{2} E_2^2 + E_1 \cdot E_2 \cos(2\pi(f_1 - f_2)t) \quad (2.19)$$

The photocurrent responds to a field by generating a current, that is proportional to a light intensity, from eq.(2.16), so will yield a photocurrent:

$$I(t) = I_1 + I_2 + 2 \sqrt{I_1 I_2} \cos(2\pi(f_1 - f_2)t) \quad (2.20)$$

The beatnote will be observable only if the two frequencies are closer to each other than the maximum detectable frequency. Detecting the beatnote between two lasers is a typical technique to measure and even control the frequency difference between two lasers. It is useful to use the Allan deviation and the power spectral density to have a complete stability and noise measurements.

The previous treatment is done for monochromatic electric fields, when the linewidth is equal to zero, while if an additive phase noise is present, it will affect the beatnote. Thus, the beatnote is a method to measure the phase noise difference between the two lasers used.

Chapter 3

Laser setup and beatnote generation

The thesis aim is the frequency characterization of the diode laser used in the pulsed optical pumped clock (POP). The frequency stability of the Rb atomic clock depends on the noise of the laser used, so, measuring the laser frequency noise spectral density and stability is a necessary step for a full characterization of the clock and for possible improvements of the clock performances.

The laser diode from Eagleyard is characterized in terms of frequency noise, using a fiber laser with narrower linewidth as a reference. In order to do this characterization a difference in frequency using the beatnote method is done. Thus, the two laser beams are correctly overlapped with the optic setup.

The fiber laser used is the low-noise single-frequency Koheras ADJUSTIK K822 made by the NKT Photonics, C15 model (Co-doped Erbium/Ytterbium fiber laser), in figure 3.1. It has a wavelength of 1560 nm, a power setpoint of 10 mW and a maximum modulation bandwidth of 1 kHz. The fiber laser is tuned on the same line of the Rb thermally and the stabilized condition is obtained by the input voltage modulation. This is used combined with a continuous wave (CW) amplifier, the Koheras Boostik High Power Amplifier (HPA), necessary to amplify the optical power produced by the laser, which contains reliable, high-brightness diode lasers. Also, there are a heat sink and a fan to prevent possible overheating [64].

The fiber laser blocks are represented in red in figure 3.2.



Figure 3.1: Koheras ADJUSTIK K822 NKT Photonics.

3.1 Fiber laser stabilization system

The stabilization system tunes the laser frequency to the Rb resonance and is represented by the blue blocks reported in figure 3.2. A Second Harmonic Generation crystal (SHG), which has an input wave at a defined frequency in a nonlinear material, produces in output a wave with twice the optical frequency. Therefore, the Koheras narrow linewidth laser converts the 1560 nm to 780 nm [57].

In particular, the laser system has a branch that goes to a saturated absorption spectroscopy (SAS) setup to stabilize it on an external cell, while another one goes to the beatnote setup, represented by the green block in figure 3.2.

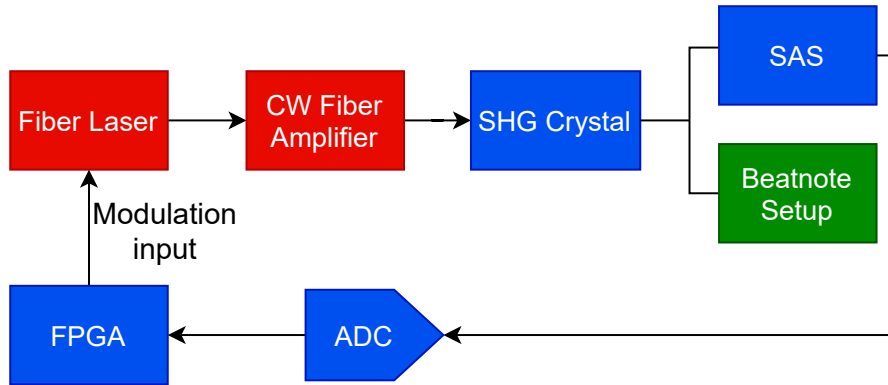


Figure 3.2: Fiber laser stabilization setup.

The saturated absorption spectroscopy setup (SAS), reported in figure 3.3, receives as input the optical beam by the SHG crystal, that is sent to a reference vapor cell filled with ^{87}Rb for performing the spectroscopy. The first reflection on the polarized beam splitter is the pump beam while the probe is the counter-propagating

beam, generated by the retro-reflecting mirror. The polarization are crossed due to the $\lambda/4$ effect.

On the other hand, the absorption signal is detected by a photodiode whose output is digitized by an analog-to-digital converter. This signal is processed by an FPGA, which implements a digital lock-in and modulates with a square wave at frequency modulation up to 200 Hz.

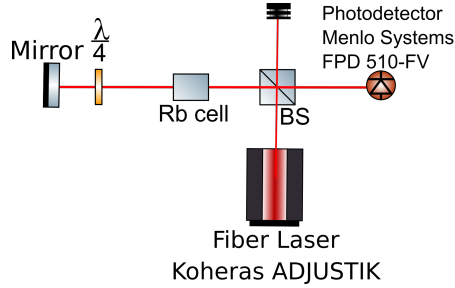


Figure 3.3: Fiber laser spectroscopy setup.

3.2 Beatnote setup

The beatnote is generated doing the difference in frequency between two laser diodes and fiber laser sources, using the heterodyne detection. The optics occupy roughly $40\text{ cm} \times 40\text{ cm}$ of optical breadboard, so every choice is done to respect these dimensions.

The optical elements necessary to generate the beatnote are shown in figure 3.4.

- Laser diode with serial number SN FB-04038;
- fiber laser Koheras Adjustik K822 NKT Photonics;
- a flip mirror and four mirrors;
- convex lenses of $F=+125$ and $F=+50$;
- concave lens of $F=-50$;
- filter NE40A-B;
- three $\frac{\lambda}{2}$ layers;
- two polarized beam splitter PBS12-780;
- a fiber collimator F110APC-780;
- a photodiode Menlo System FPD510-FV.

The DFB has an NTC sensor to control the temperature with a Peltier, it operates with a setpoint of 96 mA at 22 °C. The beam arrives at the first flip mirror at

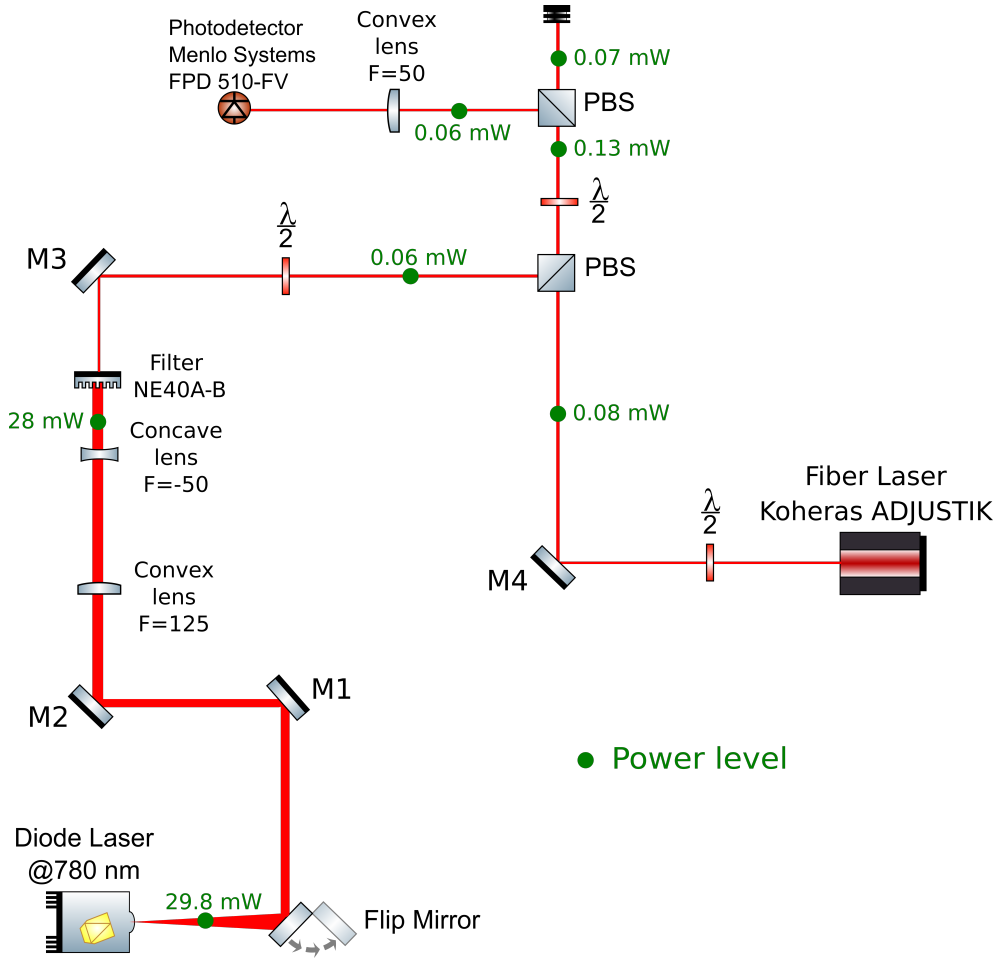


Figure 3.4: Optical circuit.

6.4 cm height. Thus, the flip and two mirrors, M1 and M2, are used to keep the correct height and horizontal dimension of the DFB ray and to change its direction respecting the area available.

A telescope is used to re-collimate the beam and to reduce its waist by a factor. It is made by two lenses, the first is a convex lens with a focal $F = +125$ to reduce the beam scattering and the second is a concave lens $F = -50$, to produce the correct beam dimension. This ray arrives at a polarized beam splitter, that gives contributions on both the transmitted and reflected directions. The DFB ray is p-polarized, but inserting a $\lambda/2$ it is possible to change the polarization to the s, and having at the output a signal of total reflections, equal to the 99% of the inputs. On the other hand, the fiber laser Koheras Adjustik K822 NKT Photonics is connected to a collimator, F110APC-780, that gives to the beam the correct direction. Also, a $\lambda/2$ is inserted to optimize the transmission through the PBS

(*p*-polarization).

A 27 dB attenuator NE40A-B is inserted after the telescope to have the same power contribution on both the two input branches of the first BS. Another beam splitter and a half wavelength are inserted in the optic setup to have the same polarization for both the two beams before the photodiode. The transmitted beam is blocked, while the reflected one is used. At last, a photodetector (PD), FPD510-FV Menlo System with a bandwidth of (0 to 200) MHz, is inserted to convert the beatnote produced from an optic to an electronic signal, with a gain of $4 \cdot 10^4$ V/W. A lens with short focal length 50 mm is used to focus the beam on the active area of the PD. A power analysis is done using the power meter, PM100A Thorlabs, in figure 3.4, on both arms of the first PBS the power is around $60 \mu\text{W}$. The beatnote is observed and analyzed on an oscilloscope, presents a pk-pk signal of 500 mV. The beatnote frequency can be defined in a range of (5 to 200) MHz by properly tuning the frequency of the two lasers, while the frequency is exactly 80 MHz if they are stabilized on the same line. Therefore different analysis are done to determine the frequency stability.

3.3 DFB stabilization system

The relative stability for the medium-long term of the two stabilization systems is evaluated by measuring the frequency of beatnote over time and the frequency counted.

The beatnote frequency between the DFB and the fiber laser is measured with the Menlo photodiode FPD510-FV and counted with Agilent 53132A, AC-coupled, in two different configurations:

1. 10 ms gate time with sampling time $T_s = 26$ ms
2. 1 s gate time with sampling time $T_s = 1.016$ s

Both lasers can be stabilized with the dedicated saturation spectroscopy setups. The DFB is locked with analog electronics, while the fiber laser is stabilized with a digital lock-in implemented on FPGA, with a time between each correction of $T_c = 16.64$ ms. The frequency of the beatnote is 80 MHz in the case of both lasers locked on the same sub-Doppler peak (the DFB frequency is shifted by 80 MHz since the pump is up-shifted by 160 MHz with a double pass AOM, acousto-optic modulator). In the case one of the two lasers, or both, is free-running, the beatnote frequency is arbitrary, between 80 and 150 MHz.

The setup contains different components shown in figure 3.5:

- Laser diode with serial number SN FB-04038;
- temperature Controller Thorlabs TED 200;

- ULN Laser Diode Controller 100 mA Thorlabs LDC 201 C;
- function generator GW INSTRON GFG-8219A;
- dual Channel Arbitrary/Function Generator Tektronix FG 3252;
- DSP Lock-IN Amplifier Signal Recovery 7225;
- proportional integral control;
- photodiode Menlo System FPD510-FV;
- programmable DC Power Supply Rigol DP831;
- universal Counter Agilent 53132A;
- acousto-optic modulator (AOM).

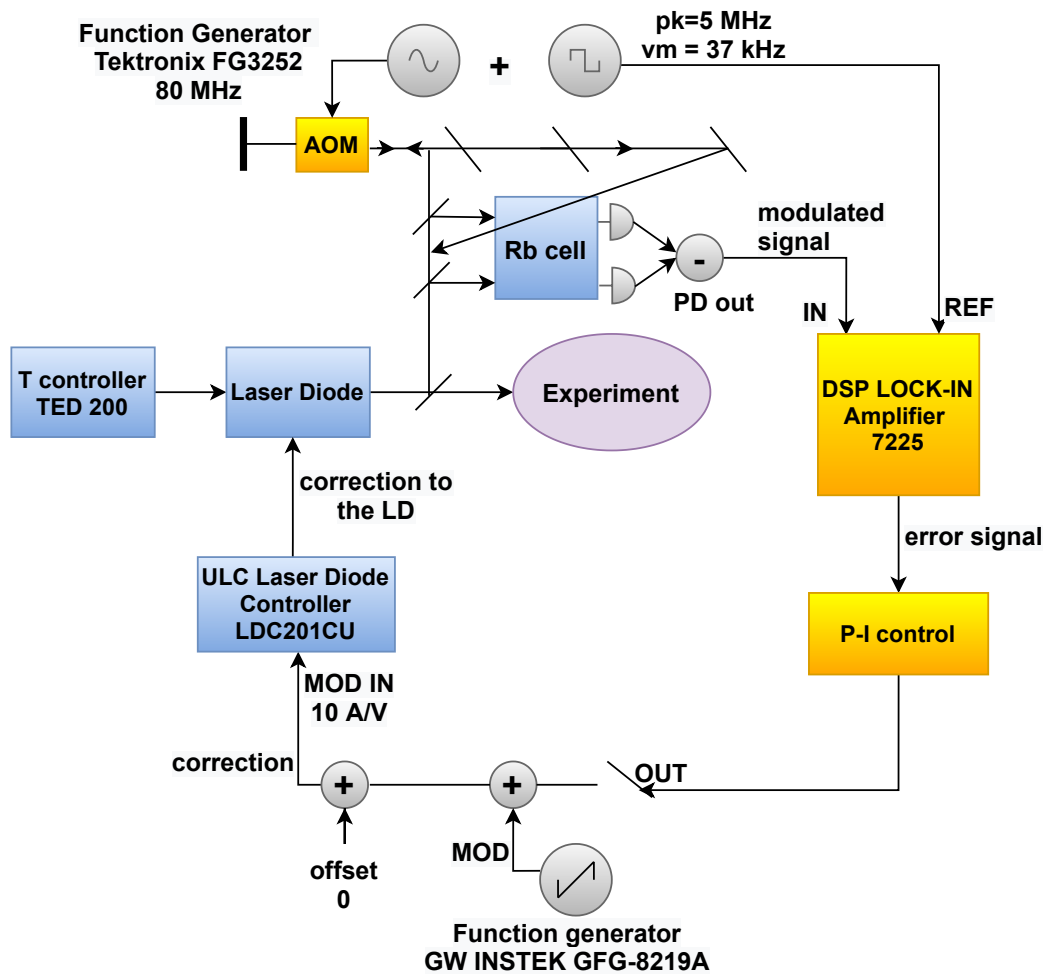


Figure 3.5: Frequency stabilization setup.

The pump is frequency shifted by 80 MHz since the pump is up-shifted by 160 MHz with a double pass AOM and superimposed to one of the two probe beams almost

counter-propagating. Thus, the modulation is introduced on the pump beam by the AOM. The transmission through the cell is detected with a differential photodiode. The lock-in takes as inputs the modulated signal given by the photodiode and the reference one by the function generator and generates an error signal. Thus, the P-I controller takes this signal and gives in output a correction, which the current driver provides to the laser diode. The DFB is also controlled in temperature by the T controller TED 200.

The frequency noise characterization will be characterized in two ways. The DFB frequency noise measurement using the frequency-to-voltage converter and the analysis of noise contributions are described in chapter 4. The laser stabilization setups are instead characterized in terms of long-term frequency stability in chapter 5.

Chapter 4

DFB frequency noise measurement

The short-term stability is influenced by all the noise sources that impact the clock signal. The noise inputs can be characterized by using the power spectral density. Then, converting the frequency noise into a voltage one is necessary to measure it easily with a spectrum analyzer. The beatnote signal has a big phase noise, and it is not possible to measure it with a phase-meter. The lasers have noise well above the typical noise of the synthesizer, which is -134 dBc/Hz in the range of frequency 250 kHz to 250 MHz.

Therefore, the frequency to voltage converter EB190211 developed in INRIM to do the measurements is used. This one has a sufficient sensibility and low noise to measure the laser diodes spectra, and also the f/V converter behavior is not limited by the spectrum analyzer.

4.1 Frequency/Voltage converter

Two methods can be used to have a frequency measurement. The first is based on a digital frequency counter, that measure directly the frequency. While the second method is relied on the f/V converter and a consequently voltage measurement. The EB190211 developed at INRIM uses the f/V technique, which is based on the mean value of a series of pulses. The device receives at one input a sinusoid through a flip-flop and at the second input the same signal but delayed by a line. The signal passes through a NAND, used as its reset '0', which receives the flip-flop output and the delayed input, as reported in figure 4.1. At every zero crosses, this device transforms the input signal in a train of pulses at fixed area of equal frequency. The area is defined as constant width multiplied by fixed amplitude and its width is determined by a self-resetting mechanism.

The series of impulses arrive at a low-pass-filter (LP) that averages the standard pulses, and produces an output voltage proportional to the input frequency [65]. This method has a fast f/V conversion and high uncertainty. The frequency/voltage converter needs a voltage power supply of 5 V, with an optimal working point of 12 or 13 dBm for the input signal, but it can work up to -6 dBm. It has a range of (1 to 210) MHz and an acceptable output voltage of (0 to 3.3) V. The f/V converter is calibrated and then its residual noise is measured to understand the impact on the laser frequency noise measurement.

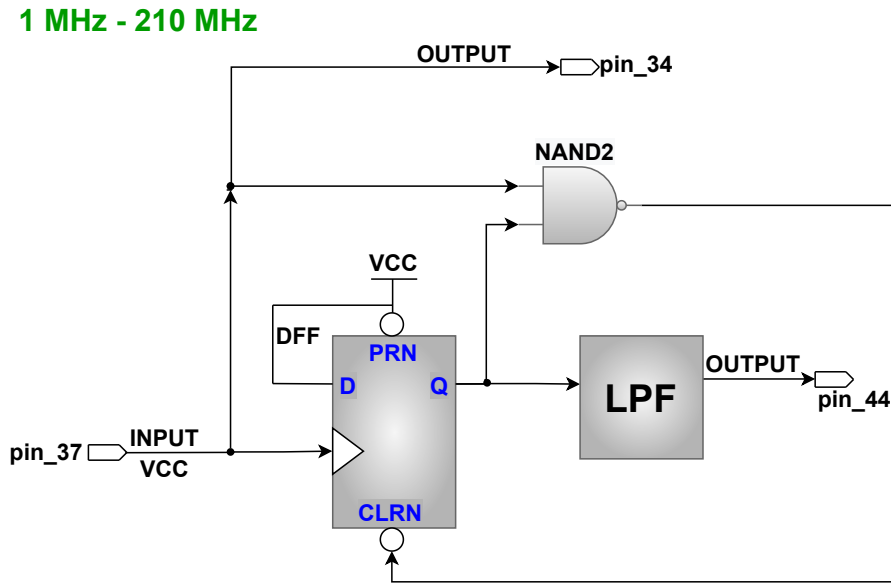


Figure 4.1: f/V converter scheme.

4.1.1 Calibration

The f/V converter gives a voltage proportional to the input frequency. An output voltage as a function of the input frequency is interesting, therefore the device is calibrated. For this reason, a synthesizer is used to give a frequency sweep in input and a multimeter is employed to obtain the measurements in output.

The converter is calibrated using as input a sinusoid at different frequencies, in the range of (1 to 210) MHz and to produce at the output a voltage in the range of (0 to 3.3) V. To measure the conversion between input frequency and output voltage and thus calibrating the instrument, the setup reported in figure 4.2 has been used.

- f/V converter EB190211;
- DC power supply Agilent E3632A;
- pulse/arbitrary Waveform Generator Siglent SDG6032X, 350 MHz and 2.4 GSa/s;
- 6 ½ Digit Multimeter 34461A;
- digital Oscilloscope Rigol DS1104Z.

The converter input is connected with a power splitter to the function generator and also with an oscilloscope to monitor the signal. While the output is connected to a multimeter to measure the output voltage as a function of the synthesizer frequency.

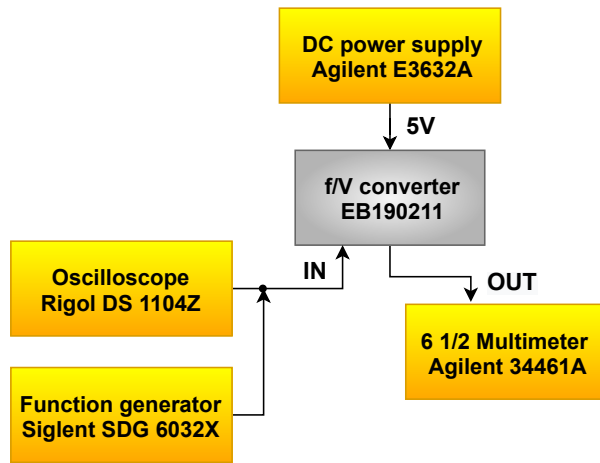


Figure 4.2: Frequency to voltage converter calibration.

In particular it is analyzed the condition of the beatnote at 80 MHz with an amplitude of about 500 mVpp, which corresponds to -2 dBm power level. The analysis is repeated also at different input powers, to have a complete characterization of the device behavior. The calibration curve is retrieved by performing a least-square method. A linear behavior is assumed and checked by looking at the residuals in figure 4.3. On the other hand, the m and b coefficients of the fitting curve $y = mx + b$ are estimated to characterize the device.

On the top, it is possible to notice the experimental data and the curve extracted from the least-square algorithm, while at the bottom there is the residue evaluation of $V_{measured} - V_{fit}$.

The coefficient measurements and the mean estimation are done for different amplitude voltages, which corresponds to interesting power values for the characterization, in the table 4.1.

Given that the values are consistent within the uncertainty, a mean of the different

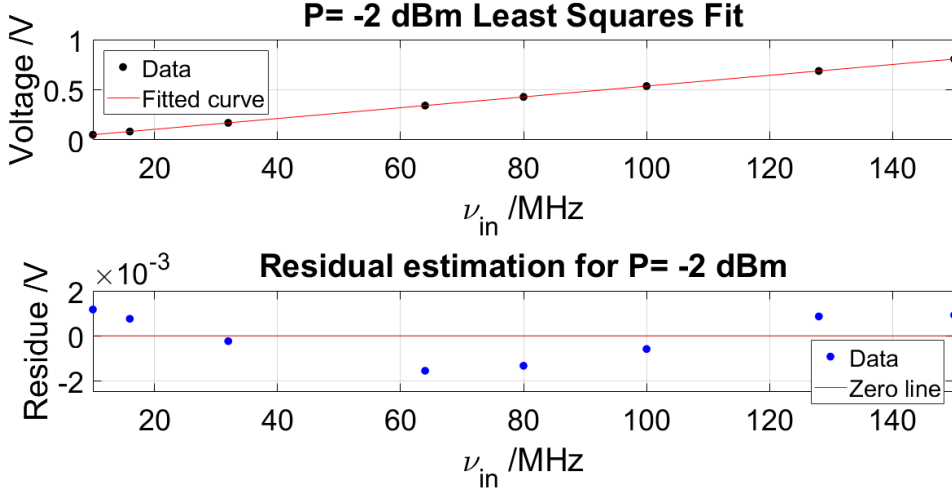


Figure 4.3: Fitting and residue of -2 dBm curve.

Power /dBm	m /(V/MHz)	b /V
+0.88	0.005375(1)	-0.00084(3)
+6	0.005387(1)	-0.00183(3)
-2	0.005387(1)	-0.00189(3)
-6	0.005397(1)	-0.00219(3)

Table 4.1: f/V converter coefficients.

values is taken. The f/V converter sensitivity coefficient obtained is equal to 5.4(1) mV/MHz.

The f/V converter has a range of (1 to 210) MHz by construction, but it is checked if the linear behavior was maintained in the whole range as reported in figure 4.3. As a function of the carrier frequency ν_c , the voltage $V = V_{measured} - b - m \nu_c$ is evaluated over the whole theoretical bandwidth. While V_{fit} represents the values of the fitting curve extracted from the data measured. Therefore, the converter deviation from linearity considering all the power cases is reported in figure 4.4. The ratio of $\frac{V}{V_{fit}}$ represent the deviation of values measured with the multimeter from the theoretic fitted ones, which are retrieved by performing the least-square method.

Following this analysis, the acceptable working range of f/V converter is considered in the region from 10 MHz to 150 MHz, where the non linearity is less than 0.1 dB.

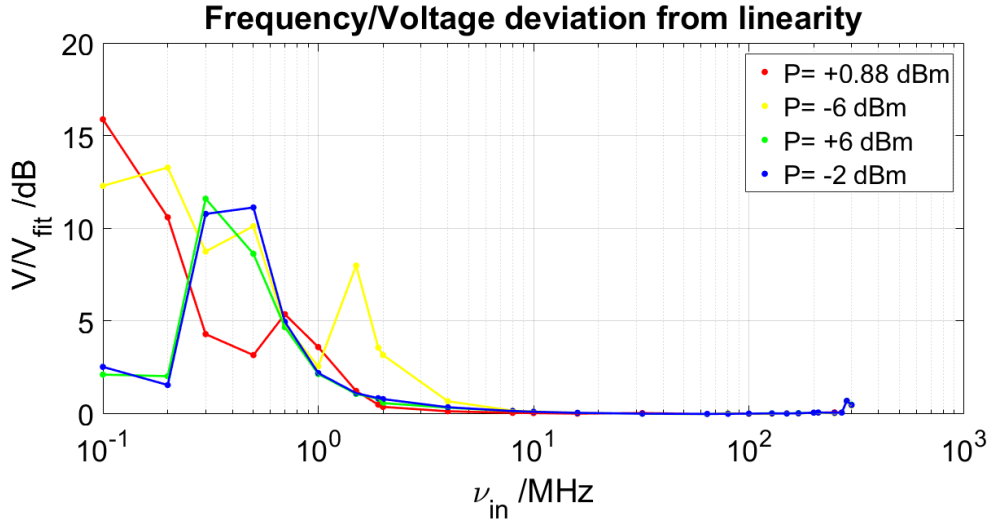


Figure 4.4: f/V converter deviation from linearity.

4.1.2 Characterization

To estimate the instrument noise, a stable signal made by a synthesizer, Agilent E8257D, with a low noise floor is provided. The measurement setup is shown in figure 4.5:

- f/V converter EB190211;
- DC power supply Agilent E3632A;
- dynamic Signal Analyzer Agilent 35670A;
- analog Signal Generator Agilent E8257D, 250 kHz to 20 GHz;
- low-noise amplifier based on LT1028;
- programmable DC Power Supply Rigol DP832A.

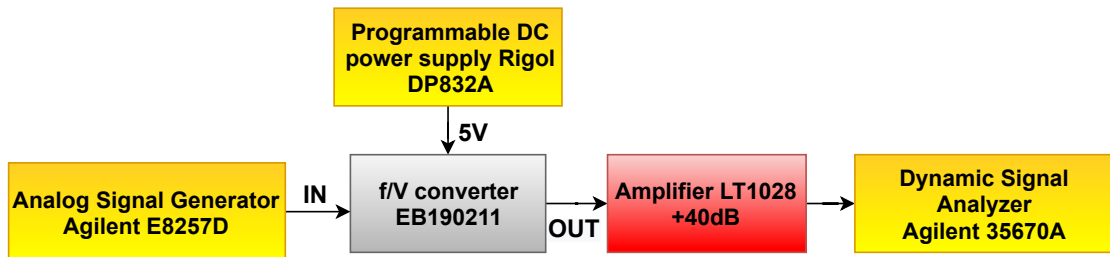


Figure 4.5: f/V characterization scheme.

From the datasheet of the synthesizer [66], the typical phase noise values for different carrier frequencies, in dBc/Hz, are taken into consideration and so converted into

frequency noise, in table 4.2.

f /Hz	L /dBc	S_φ / (dB rad ² /Hz)	S_ν / (dB Hz ² /Hz)
1	-66	-63	-63
10	-94	-91	-81
100	-120	-117	-97
1000	-128	-125	-95
10000	-132	-129	-89
100000	-133	-130	-80

Table 4.2: Analog Signal Generator Agilent E8257D noise.

The spectrum analyzer noise floor is measured as reported in eq.(4.1).

$$\text{NF}_{\text{SA}} = -154 \text{ dB} \frac{\text{V}^2}{\text{Hz}} \quad (4.1)$$

The characterization of the f/V converter is done changing the frequencies, in octave from 10 MHz to 160 MHz and the analysis is repeated for different inputs, like ± 6 dBm and 12 dBm. The LT1028 is used not to be limited by the measurement-system noise floor, so amplify of +40 dB the signal.

The voltage noise is measured at different frequencies and power at the output of the amplifier, so a typical measurement with input power equal to 12 dBm, is shown in figure 4.6. The values obtained are converted into frequency noise knowing the calibration curve.

$$S_\nu(f) = \frac{1}{m^2} S_V(f) \quad (4.2)$$

where m is the converter sensitivity coefficient.

For completeness, fixing the signal generator to the beatnote frequency $\nu_c = 80$ MHz, the f/V noise floor is reported in figure 4.7 at different power estimations. The noise decreases with the carrier frequency, about 6 dB/oct such as a flicker noise. At 1 kHz the voltage noise is about -133 dB V²/Hz, which corresponds to 32.4 dB Hz²/Hz, smaller than the NF_{AS} , so the f/V behavior is not limited by the spectrum analyzer. Nevertheless the analysis is repeated for different inputs on the f/V converter but the noise remains almost equal at $\nu_c = 80$ MHz as shown in figure 4.7.

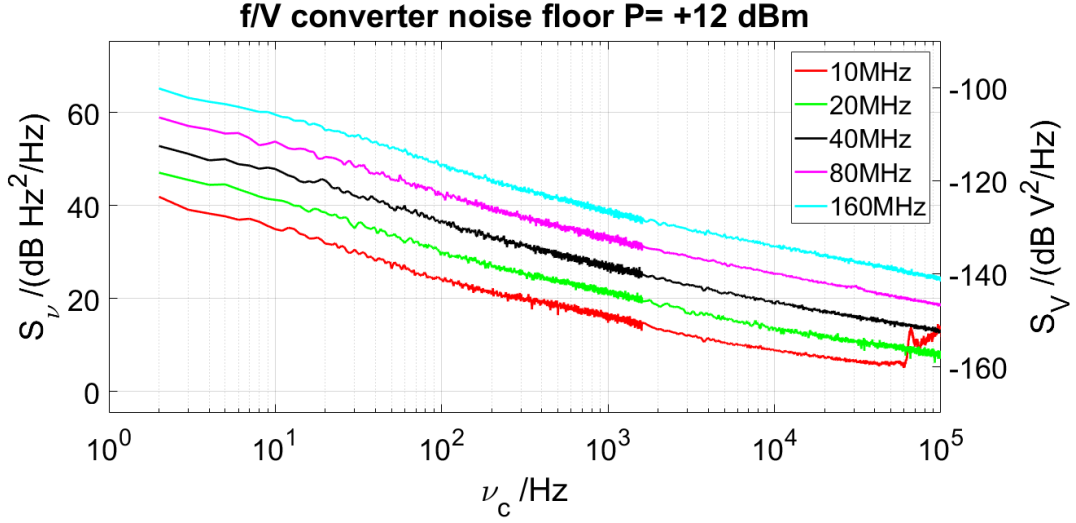


Figure 4.6: f/V noise floor with $P = +12$ dBm at different frequencies.

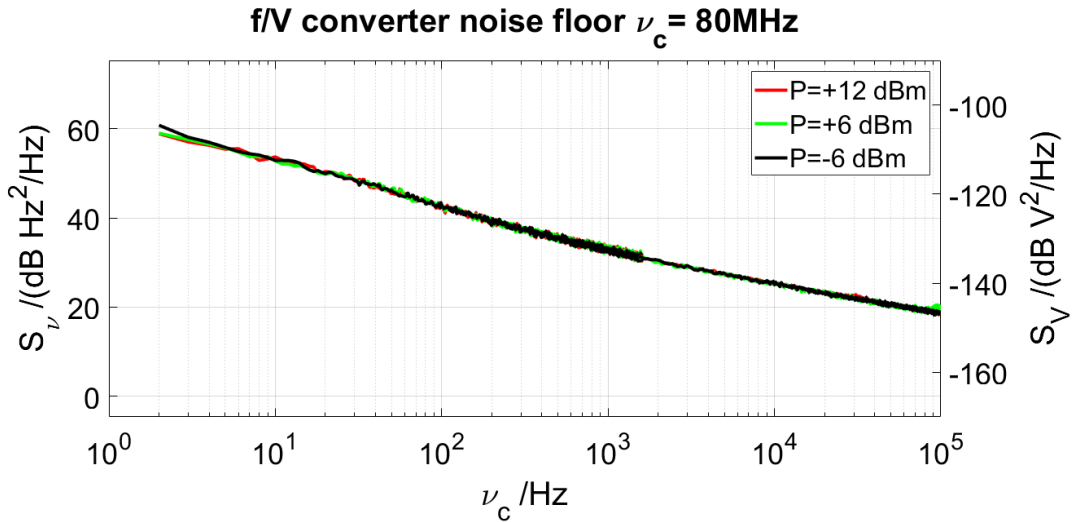


Figure 4.7: f/V noise floor with $\nu_c = 80$ MHz at different power values.

4.2 Beatnote frequency noise

The aim is the frequency stability measurement of the Rb atomic clock but depends on the noise of the laser used, so measuring the laser frequency noise is necessary to a full characterization.

The clock signal noise sources influence the short-term stability and can be characterized using the power spectral density. Therefore, the beatnote frequency noise

is measured using the converter analyzed before, due to the voltage to frequency conversion and its low noise to measure the laser diodes spectra.

The beatnote at 80 MHz is given to the f/V converter, which has a conversion coefficient of 5.4 mV/MHz, so a signal of 430 mV is produced. Thus, the voltage noise is observed in the spectrum analyzer and then converted into frequency noise. The scheme is reported in figure 4.8.

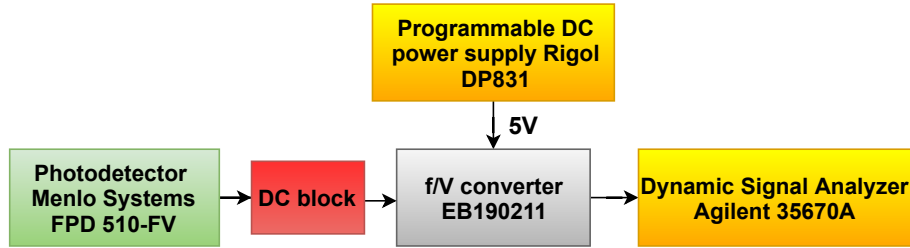


Figure 4.8: Beatnote measurement scheme.

The photodetector FPD 510-FV converts the optic signal into a current and it is connected to the converter input with a direct current (DC) block. The latter is used to remove the DC component of the beatnote signal. In fact, the f/V converter evaluate the zero-crossing so a sinusoidal signal centered at zero is given and the DC component is removed. At the output there is the SA Agilent 35670A, that it is needed to observe the power spectral density.

The DFB is locked on the $F = 2 \rightarrow F' = 2,3$ transition with a current control fixed to $I_{current} = 94$ mA and at the temperature 22°C . The error signal corresponding to that line is reported in figure 4.9, and also others lock-in lines and crossover of ^{87}Rb hyperfine energy levels are represented.

At first, the FFT SA noise floor is measured, at different spans, connecting a $50\ \Omega$ termination. The beatnote is measured considering both the DFB and fiber laser in free-running and also the case of fiber laser in free-running and laser diode stabilized on the Rb cell. The same measurements are repeated with the fiber laser locked and the DFB in free-running.

To frequency-stabilize the fiber laser, it is modulated with a modulation depth of 5 MHz, with a square wave at frequency 120.48 Hz (8.3 ms period). The loop bandwidth is calculated as $B = \frac{1}{2\pi\tau} = 200$ Hz, where $\tau = 800$ ms is measured using the (10 – 90)% method. The error signal when an offset is given to it and then the stabilized loop is closed, is reported in figure 4.10.

The measurements are also done with both fiber laser and DFB locked. The beatnote noise in different locking conditions at the carrier frequency $\nu_c = 80$ MHz is represented in figure 4.11.

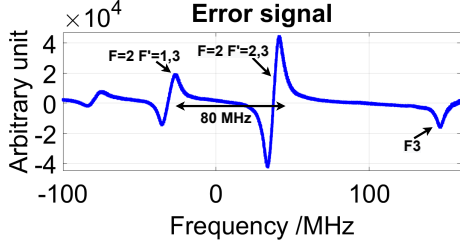


Figure 4.9: SCAN error signal of ^{87}Rb energy levels.

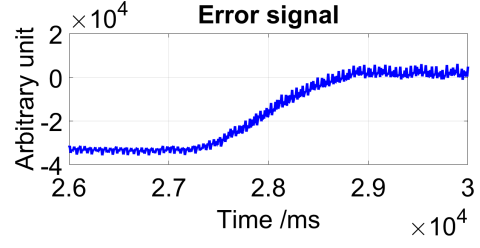


Figure 4.10: Error signal with closed stabilized loop.

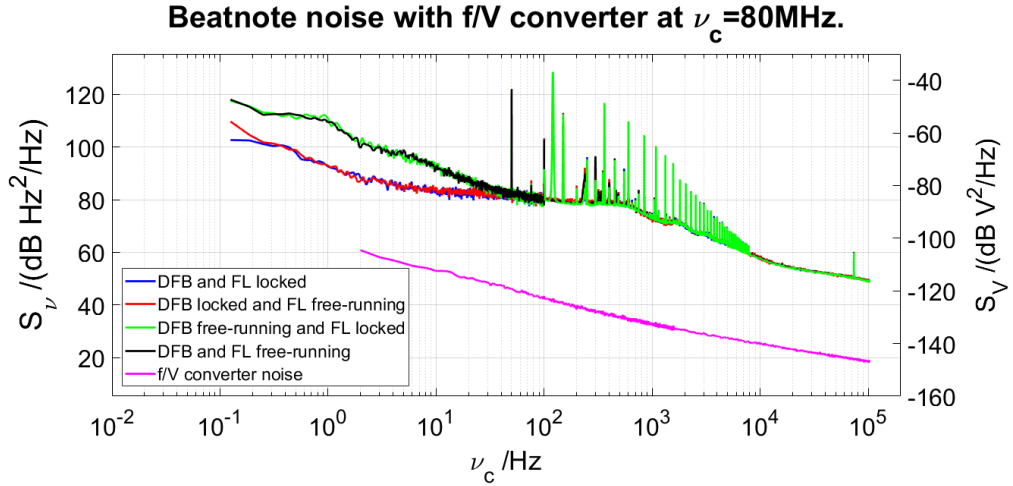


Figure 4.11: Beatnote noise at $\nu_c = 80$ MHz.

From figure 4.11 is deduced that the fiber laser in free-running does not limit the measurements, it is not necessary to stabilize it for noise from tens of mHz up, due to the higher behavior of the DFB.

In the frequency noise curve a plateau is observed at 100 Hz where the frequency noise is equal to $78 \text{ dB Hz}^2/\text{Hz}$ for all the DFB and FL combinations, but for higher frequencies it goes down almost like a flicker noise. On the other hand, for frequencies higher than 50 Hz, above the locking bandwidth, open and closed loop match. It seems that the fiber laser can be considered as a reference because lock-in does not influence the stabilized condition. Also, in the case of fiber laser locked, different spurious are present due to the lock-in modulation.

Using the frequency noise spectrum measurement, the linewidth of the laser diode is measured equal to 2 MHz, while the fiber laser has a narrower linewidth of 50 kHz.

4.2.1 Effect of power-line on the frequency noise

The beatnote noise is affected by different factors such as the power line noise. Therefore, due to laboratory changes a new uninterruptible power supply (UPS) is used to see how the frequency and voltage noise can be affected.

The measurements of both lasers in free-running are re-done because a new power line is used, so it is verified that there isn't an appreciable difference on the noise levels of the two UPS. This difference is -1 dB in the range 100 Hz to 1 kHz, with more noise at multiples of the power line frequency as reported in figure 4.12.

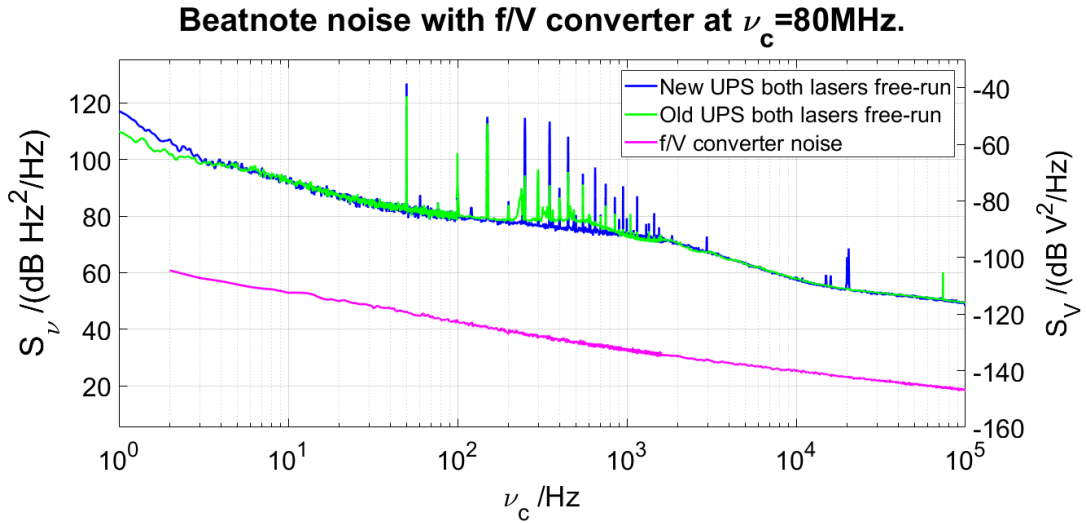


Figure 4.12: Beatnote noise at $\nu_c = 80$ MHz with different UPS.

4.3 DFB laser frequency noise measurement

During the thesis we also investigate if a different laser diode, from the same company, exhibits the same noise spectrum. Thus it is decided to change it with the DFB SN FB-04036 made by Eagleyard.

The current controller is set at 95 mA and the temperature to 22 °C, to be resonant with the $F = 2 \rightarrow F' = 2,3$ line. These parameters are very similar to the ones of the latter diode. Then, a power analysis with the PM100A Thorlabs power meter is done to see that the contributions are almost the same.

The frequency noises measured with the two different laser diodes have almost the same behavior with a small difference at high frequencies as shown in figure 4.13. Therefore, it is decided to go ahead with the measurements using the SN FB-04036.

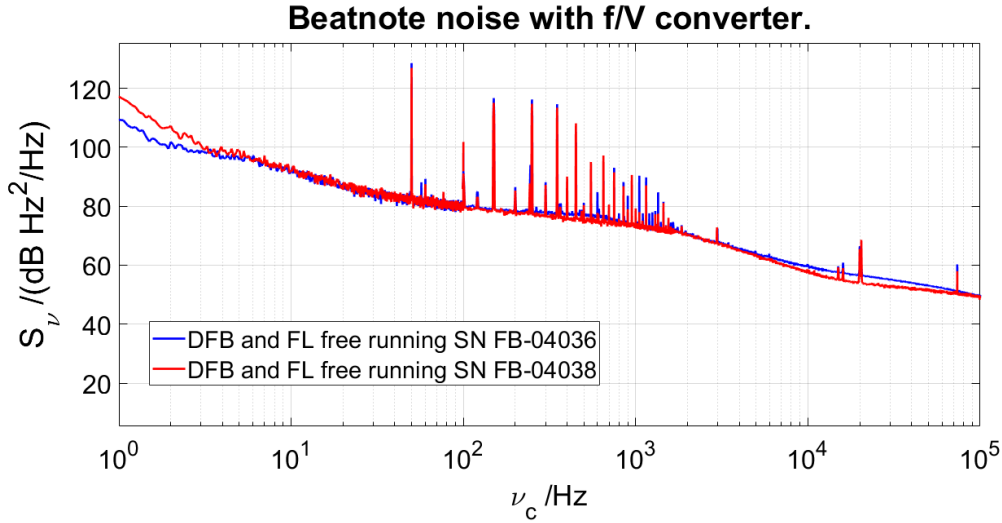


Figure 4.13: Beatnote comparison between two different DFB.

4.4 Current driver contribution

The frequency noise measured before could suffer from a contribution of the current driver. To check if what is measured is the intrinsic noise of the diode, it became necessary to study the laser current stability and find the driver noise contributions.

4.4.1 LDC201CU driver

At first, the LDC201C ULN laser diode controller used so far is characterized. The monitor measurement of the LDC201CU is done in the case of the laser diode as load. The monitor output of the driver (CTL OUT) is used to measure the current noise while the driver is operational. This one has an amplification of 100 V/A with a voltage partition, $\frac{R_2}{R_1+R_2}$ directly connected to the spectrum analyzer to see the voltage noise. While the load output (LD OUT) of the driver is connected to the DFB SN FB-04036 as load, as reported in figure 4.14. The current driver gives 95.25 mA, thus the output of monitor gives 9.46 V, while after the voltage partition there is only 4.72 V, equal to have a 6 dB attenuation. The FFT SA has an AC coupling and the input range is set to 3.9 mVpk for all the span.

The measurements are done using the resistance $R_1 = R_2 = R = 10.15 \text{ k}\Omega$ in the case of laser diode in free-running or locked on the Rb cell, as shown in figure 4.15.

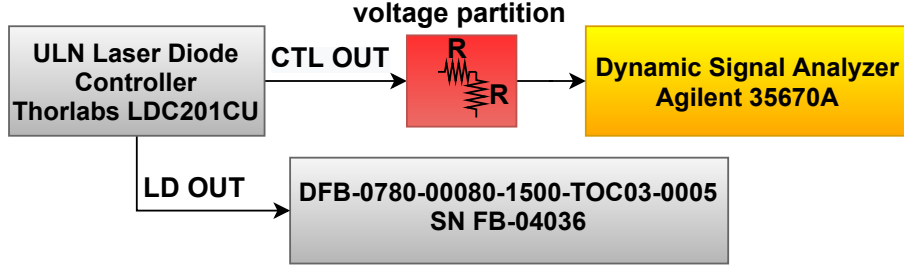


Figure 4.14: LDC201CU monitor output with a voltage partition.

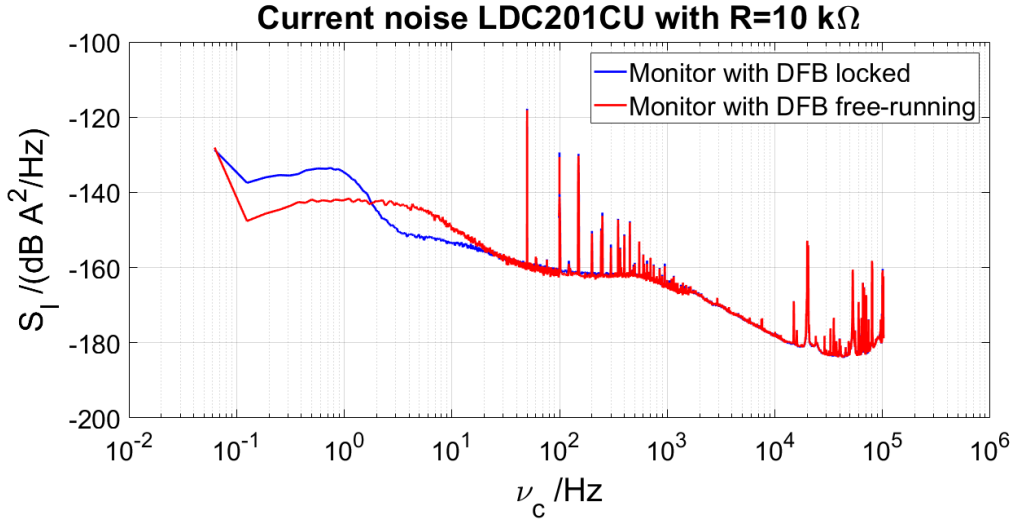


Figure 4.15: LDC201CU monitor output current noise.

The monitor output of LDC201CU with the DFB as termination at 1 kHz has a voltage noise of $-128 \text{ dB V}^2/\text{Hz}$. To this value is subtracted the amplifier gain of 40 dB and it is converted the voltage to current using the the coefficient 100 V/A . The current noise in $\text{dB } \frac{\text{A}^2}{\text{Hz}}$ is estimated from the voltage one. The effect of the current noise on the laser frequency noise is interesting, so the current-to-frequency conversion coefficient is estimated. The frequency noise spectrum in $\text{dB } \frac{\text{Hz}^2}{\text{Hz}}$ is equal to the current-to-frequency conversion coefficient multiplied by the current noise spectrum, in eq.(4.3).

$$S_\nu = \left| \frac{\delta\nu}{\delta I} \right|^2 \cdot S_I \quad (4.3)$$

Measuring the current setpoint when the laser is locked on different sub-Doppler dips, and knowing the frequency difference between the dips from the Rb level scheme, the current-to-frequency coefficient is derived.

In the case of $F = 2 \rightarrow F' = 1,2$ transition and $F = 3$ the currents of the two

peaks are measured, obtaining the values in eq.(4.4):

$$I_{X2,3} = 95.3 \text{ mA} \quad I_{X1,2} = 86 \text{ mA} \quad (4.4)$$

The experimentally current-to-frequency coefficient, in eq.(4.5), is evaluated using the peaks frequency difference of $\Delta\nu = 7.046457 \text{ GHz}$, estimated from the ^{87}Rb D_2 transition hyperfine structure, with frequency splittings between the hyperfine energy levels [67].

$$\frac{\Delta\nu}{\Delta I} = \frac{7.046457 \text{ GHz}}{9.21 \text{ mA}} = 765 \frac{\text{MHz}}{\text{mA}} \quad (4.5)$$

All the current noise measurements are scaled using the measured coefficient in eq.(4.5).

This one is used to calculate the current driver contribution reported in figure 4.16. Also in table 4.3 there are reported the voltage, current and frequency noise measurements at different frequencies.

Frequency	Voltage noise	Current noise	Frequency noise
100 Hz	-124 dB $\frac{\text{V}^2}{\text{Hz}}$	-161 dB $\frac{\text{A}^2}{\text{Hz}}$	76 dB $\frac{\text{Hz}^2}{\text{Hz}}$
1 kHz	-128 dB $\frac{\text{V}^2}{\text{Hz}}$	-165 dB $\frac{\text{A}^2}{\text{Hz}}$	73 dB $\frac{\text{Hz}^2}{\text{Hz}}$
10 kHz	-141 dB $\frac{\text{V}^2}{\text{Hz}}$	-178 dB $\frac{\text{A}^2}{\text{Hz}}$	60 dB $\frac{\text{Hz}^2}{\text{Hz}}$

Table 4.3: LDC201CU noise at different frequencies.

4.5 Contribution of the current generator to the frequency noise

After the current driver analysis, a comparison between this measurement and the beatnote one is done, to understand if the latter could be limited by the driver noise.

The beatnote measurements at $\nu = 80 \text{ MHz}$ are compared to the frequency noise of the LDC201CU monitor output in the two cases of DFB locked and in free-running, as reported in figure 4.16. The fiber laser is considered as a reference because its behavior is equal for every condition, so it is reported only the free-running one.

The characteristics of the laser diode are limited by the current driver. Therefore, the driver noise is not negligible but it is the greater contribution, because it is always dominant particularly above 500 Hz and also limited at the lowest frequencies. For this frequency range it is thus observed only the driver characteristics.

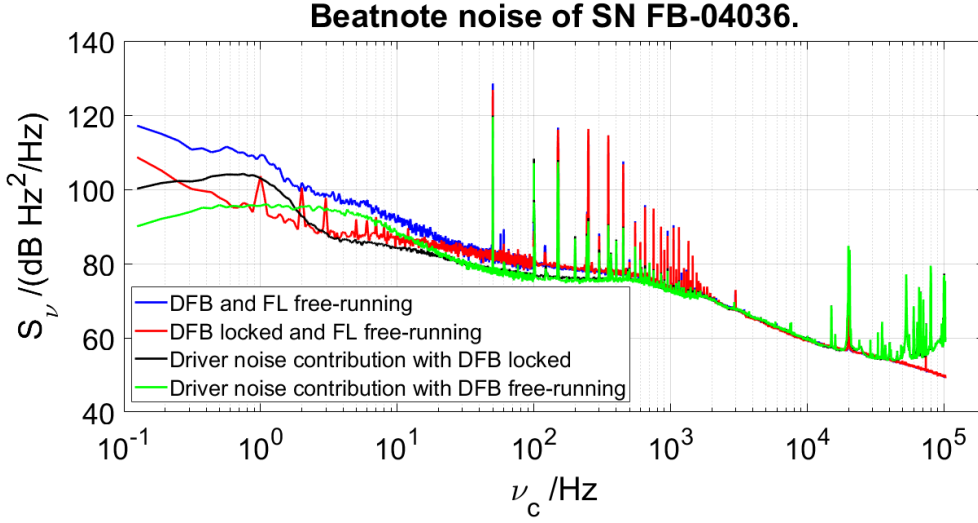


Figure 4.16: Frequency noise of the beatnote and driver noise contribution.

To properly estimate the intrinsic noise of the DFB a driver with lower current noise must be used. Since below 1 kHz the driver noise is below the measured laser frequency noise, so the current driver contribution is subtracted, to have a closer estimate of the true laser noise.

The laser diode intrinsic noise in both the two cases of stabilization on the Rb cell and in free-running condition is computed. Thus, a subtraction of the frequency noise spectrum between the beatnote and the current driver is done to obtain the intrinsic noise, in eq.(4.6) and it is reported in figure 4.17.

$$S_{\nu, \text{intrinsic}} = S_{\nu} - S_{\nu, \text{current driver}} \quad (4.6)$$

The laser diode intrinsic noise is almost flicker of frequency for two decades, from 10 Hz to 1 kHz. For frequencies below 10 Hz the slope is steeper (between f^{-1} and f^{-2}).

4.5.1 Other current drivers

To improve the setup and to evaluate the diode intrinsic noise, others current driver are characterized. A commercial laser driver, the Laserlabs made in France and then two custom drivers, a LDC200 and a LDC201-INRIM are analyzed. The first one driver is set always at 93 mA with a 50Ω termination and a low-noise amplifier based on LT1028, as the scheme reported in figure 4.18. The amplifier is thermally isolated to prevent temperature fluctuations from adding voltage noise at low frequencies.

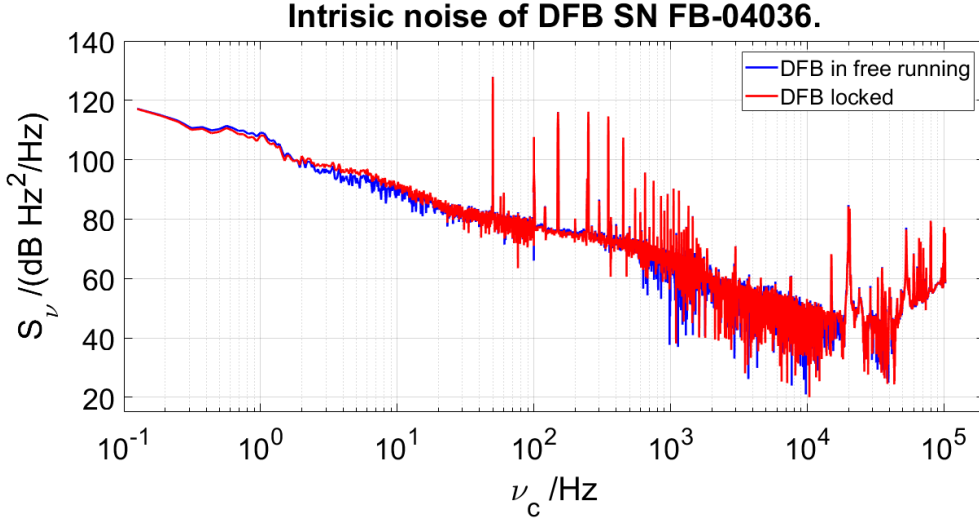


Figure 4.17: Laser diode intrinsic frequency noise.

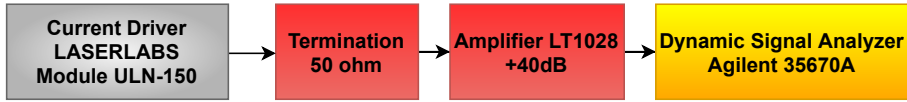


Figure 4.18: Laserlabs measurement scheme.

In figure 4.19 it is possible to see the Laserlabs current noise, which has a bump in correspondence of 1 kHz. In the table 4.4 the Laserlabs voltage, current and frequency noise at different frequencies are reported.

Frequency	Voltage noise	Current noise	Frequency noise
100 Hz	-104 dB $\frac{V^2}{Hz}$	-178 dB $\frac{A^2}{Hz}$	60 dB $\frac{Hz^2}{Hz}$
1 kHz	-93 dB $\frac{V^2}{Hz}$	-167 dB $\frac{A^2}{Hz}$	71 dB $\frac{Hz^2}{Hz}$
10 kHz	-115 dB $\frac{V^2}{Hz}$	-189 dB $\frac{A^2}{Hz}$	50 dB $\frac{Hz^2}{Hz}$

Table 4.4: Laserlabs noise at different frequencies.

Also, the two current drivers made at INRIM are characterized, the LDC200 and the LDC201-INRIM, using the same configurations as before. In tables 4.5 and 4.6 voltage, current and frequency noise values measured are listed for different frequencies of the two drivers.

Frequency	Voltage noise	Current noise	Frequency noise
100 Hz	-129 dB $\frac{V^2}{Hz}$	-163 dB $\frac{A^2}{Hz}$	75 dB $\frac{Hz^2}{Hz}$
1 kHz	-143 dB $\frac{V^2}{Hz}$	-178 dB $\frac{A^2}{Hz}$	62 dB $\frac{Hz^2}{Hz}$
10 kHz	-148 dB $\frac{V^2}{Hz}$	-182 dB $\frac{A^2}{Hz}$	55 dB $\frac{Hz^2}{Hz}$

Table 4.5: LDC200 noise at different frequencies.

Frequency	Voltage noise	Current noise	Frequency noise
100 Hz	-140 dB $\frac{V^2}{Hz}$	-163 dB $\frac{A^2}{Hz}$	75 dB $\frac{Hz^2}{Hz}$
1 kHz	-146 dB $\frac{V^2}{Hz}$	-177 dB $\frac{A^2}{Hz}$	60 dB $\frac{Hz^2}{Hz}$
10 kHz	-137 dB $\frac{V^2}{Hz}$	-182 dB $\frac{A^2}{Hz}$	56 dB $\frac{Hz^2}{Hz}$

Table 4.6: LDC201-INRIM noise at different frequencies.

Finally, a comparison between all the analyzed current drivers is done, to see which one has the lowest current and frequency noise, in figure 4.19.

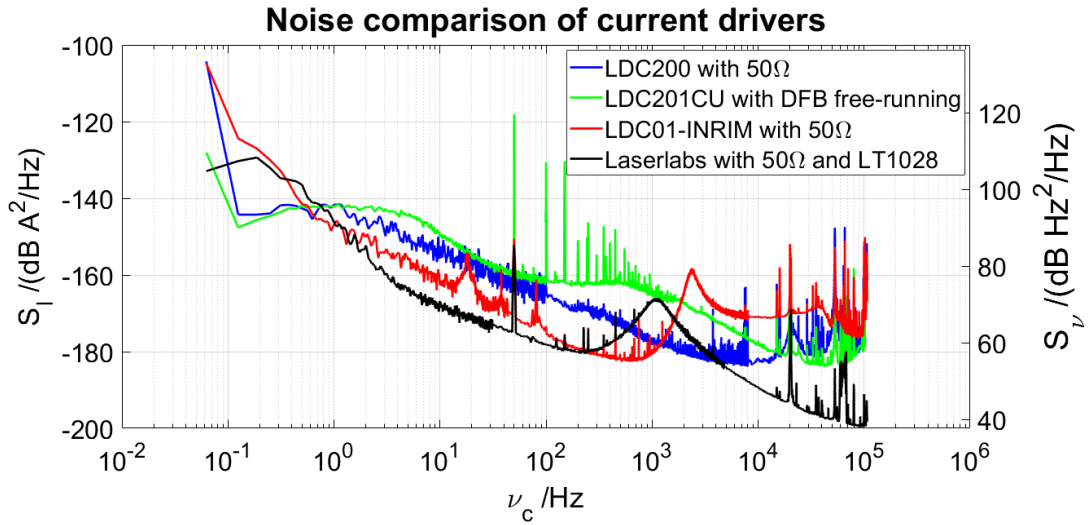


Figure 4.19: Noise comparison of current drivers. The left scale is referred to current noise in dB $\frac{A^2}{Hz}$, while the right to the frequency noise in dB $\frac{Hz^2}{Hz}$, obtained using the current-to-frequency coefficient in eq.(4.5).

The Laserlabs frequency noise is lower than the LDC201CU at low frequencies but it has a bump at 1 kHz, which causes excess noise at high frequencies. Also the LDC201-INRIM has a low current noise but with a bump at 2.2 kHz that produces excess noise among this frequency, while the LDC200 driver has lower current and frequency noise than the LDC201CU used, except at higher frequencies.

Chapter 5

Laser frequency long-term stability

5.1 Beatnote frequency characterization

The frequency noise impacts on the short-term, described before and on medium-long term. The stability of many environmental parameters starts to play a role particularly for averaging times above 1000 s. The physical mechanism by which these parameters impact the clock frequency stability are different. So, regarding the long-term performance, a careful engineering of the various components has allowed reducing some of the thermal and light-shift sensitivity coefficients. Then became interesting study this parameter, and the Allan deviation is used, which tells the frequency stability respect the time of measurement.

The laser frequency long-term stability and the impact on the POP clock are reported, to understand the laser behavior.

The beatnote at the frequency ν_0 is measured with the two lasers both in free-running, and then locked on the two spectroscopy setups in order to evaluate the two stabilization effects.

Therefore, a beatnote frequency characterization is done to find the short- and long-term stability in different setup conditions. The measurements are made using the counter Agilent 53132A at different gate times as mentioned above.

The distributed feedback laser is characterized both in free-running and stabilized configurations, with the fiber laser used as a reference in figure 5.1.

In free-running, also called open-loop (OL) configurations, for short-term stability the laser diode is predominant while increasing the time of measurement the fiber laser (FL) becomes more significant than the previous, in fact, the DFB for long-term stability exhibit flicker floor just below 1 MHz. On the other hand, in the case of both laser diode and fiber laser locked on the Rb cell, closed-loop (CL)

configuration, the Allan deviation is about two orders of magnitude at 1000 s below the case of both free-running.

The Allan deviation (ADEV) of the counter frequency measurements is calculated $\sigma_{\nu_0}(\tau)$ in Hz, in order to explain the frequency stability on the left scale. Also, relative stability is determined, referred to the laser diode frequency, as $\sigma_y(\tau) = \frac{\sigma_{\nu_0}(\tau)}{\nu_0}$ on the right scale.

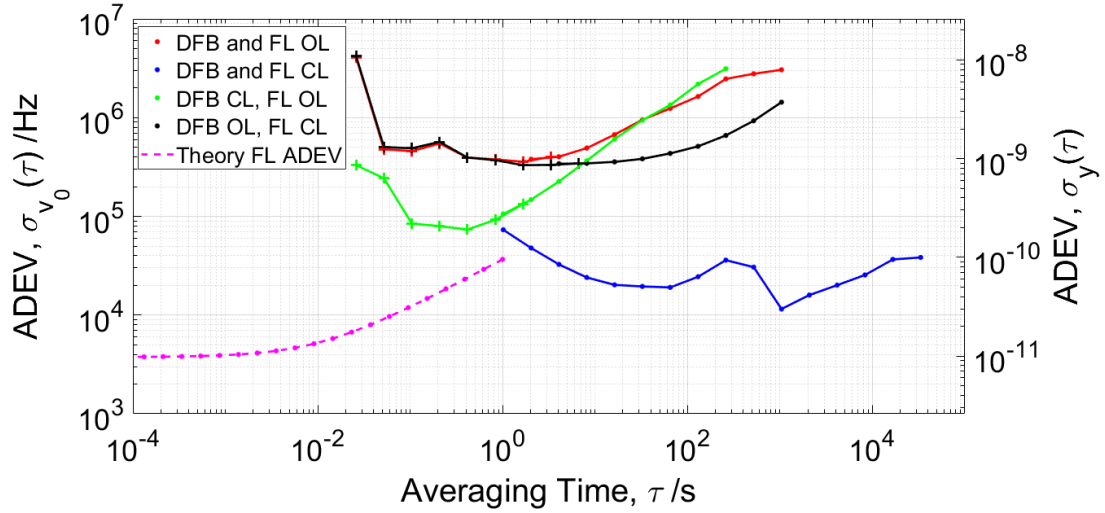


Figure 5.1: Beatnote frequency characterization. A gate time of 26 ms for times < 2 s, while equal to 1.016 s when the time of measurements is longer.

The frequency stability of the beatnote at different setup conditions must be compared with the theoretical behavior of the fiber laser, in order to understand possible limitation. So, an estimation of the frequency stability of the fiber laser is done using the frequency noise measurements on the test report, represented with the magenta curve in figure 5.1. The latter is compared with all the open-loop and closed-loop configurations of the beatnote.

Using the Adjustik test report can be extracted the phase noise levels f^{-1} and f^{-2} expressed in dB rad/ $\sqrt{\text{Hz}}$. From the test report of the Koheras Adjustik is appreciable that the laser frequency noise is measured with the delay-line method, which is 1 m optical path phase noise. Then, using the formula on the application note in eq.(2.14), the relationship between the two spectra noise is obtained, in eq.(2.15). Where τ_d is equal to $\frac{1\text{m}}{c/n}$, 1 m of optical path mismatch, c is the light velocity and $n = 1.5$ is the characteristic refractive index of the optic fiber.

The frequency noise spectrum is modelled with a polynomial sum, and the following coefficients for flicker and random-walk frequency noise are found, in table 5.1.

	Intersection with y axis	Slope
h_1	$-80 \text{ dB } \frac{\text{rad}^2}{\text{Hz}}$	f^{-1}
h_2	$-67 \text{ dB } \frac{\text{rad}^2}{\text{Hz}}$	f^{-2}

Table 5.1: Phase noise.

The spectrum can be modeled using this expression and the coefficients of frequency spectrum are derived, h_{-1} for the flicker noise and h_{-2} for the random walk noise. Therefore, the values obtained are converted into the Allan variance using the formulas derived by Rubiola [39].

$$\sigma_v^2(\tau) = A + B \cdot \tau \quad (5.1)$$

where the coefficient A and B are:

$$A = 2 \ln(2) \cdot h_{-1} \quad B = \frac{(2\pi)^2}{3} \cdot h_{-2} \quad (5.2)$$

The fiber laser behavior limits the short-term, probably due to the slow stabilization. Maybe, the bandwidth can be increased not to limit the short-term.

For short measurement time, less than 10s, both by specifications and measurements the fiber laser frequency noise is at least one order of magnitude below the DFB in both the open-loop and closed-loop configurations, so can be considered as a reference.

While for long time understanding which setup limits the stability is difficult to say a priori.

5.1.1 DFB different locking bandwidth

It is interesting to see if different locking bandwidths can provoke a changing of the error signal. The measurements with both the lasers stabilized are repeated with the laser diode locked at different proportional integral control (PI) loop gain, so means changing the sensitivity of the lock-in amplifier. Increase the latter means reduce the gain, so a noise measurement of the stabilized laser at different conditions is done to see if the laser lock-in remains equal.

The slope of a typical error signal used for locked conditions is possible to obtain. In fact, in the case of both lasers in free-running, a slow square wave is produced by the function generator INSTEK GFG-8219A and the offset of the signals are modified with the integrator. So, the error signals are observed with the oscilloscope

changing the gain of the lock-in amplifier. In the case of $S = 500 \text{ mV}$ in open loop the curve reported in figure 5.2 is obtained.

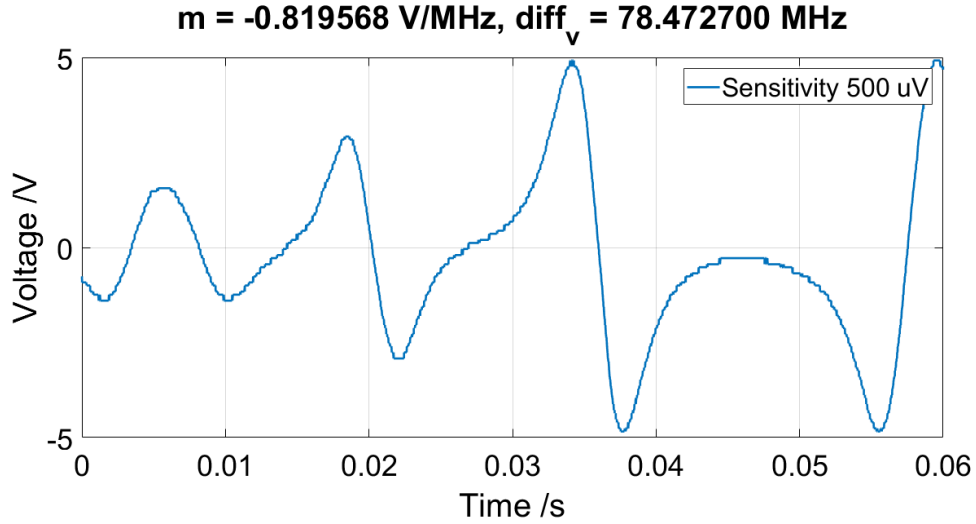


Figure 5.2: Typical error signal in open-loop.

Where, m is the slope of the error signals used to have the locked conditions, for different values of gain reported in table 5.2. Instead, the frequency difference in the middle of the two crossovers, $x_{23} - x_{13}$, is equal to 78.4727 MHz for every gain.

Sensitivity	Slope
200 μV	-1.709639 V/MHZ
500 μV	-0.819568 V/MHZ
1 mV	-0.308530 V/MHZ
2 mV	-0.196703 V/MHZ

Table 5.2: Different error signal slope.

Slope modifications of the error signals are produced by different locking bandwidths. So, the frequency stability measurements have changes due to the sensitivity coefficients employed.

5.2 POP clock frequency stability

The POP clock is influenced on the long-term by the fluctuation of the experimental parameters through different physical mechanisms [68]. One of these parameters is the laser frequency. Thus the laser medium-long term stability is important to know. To this end, the two lasers are locked to the same Rb transition on their stabilization setups. The beatnote frequency is analyzed for different days, in terms of ADEV, which gives the frequency stability of the parameter for the measurement time τ . For $\tau > 100$ s the environmental effect acting on stabilization systems starts to play a role and may limit the achievable frequency stability. Such environmental effects include temperature fluctuations that acts on the cell (causing a variation of the Rb density) and on the optics, causing possible misalignment.

A measurement of the beatnote is done using the counter, Agilent 53132A. The frequency stability, as reported in figure 5.3, is obtained with STABLE32. The measurement is repeated with the two different laser diodes tested in this thesis, both sharing the same saturation absorption setup, and they are reported in table 5.3. The same measurement is done for the two DFB diodes (red curves in figure 5.3). These show a comparison between the setups, that have some discrepancy for long averaging times.

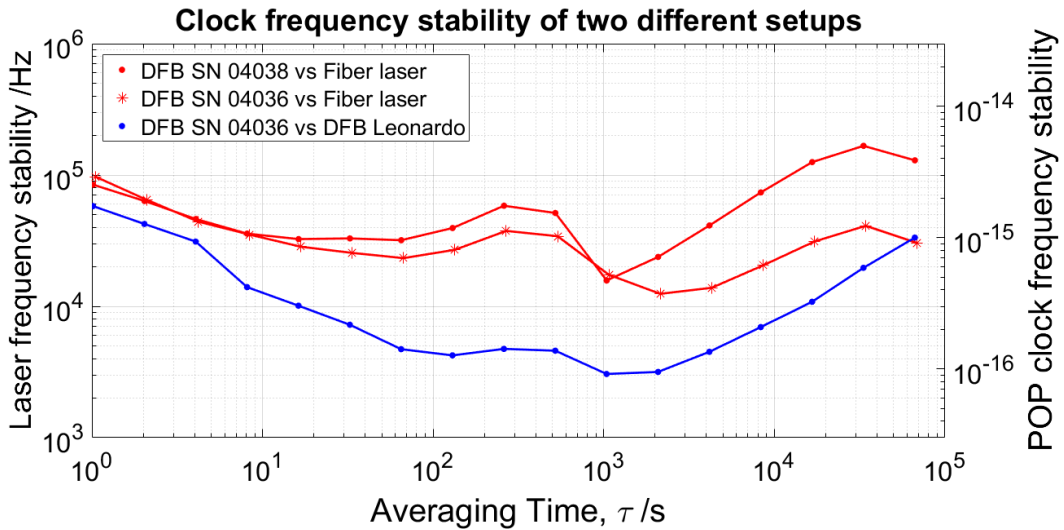


Figure 5.3: Comparison of the laser frequency stability.

The POP clock sensitivity from experimental characterization is on the order of [7]:

$$\frac{\Delta y}{\Delta \nu_L} = 3 \times 10^{-14} \frac{1}{\text{MHz}} \quad (5.3)$$

For the DFB SN FB-04036 at $\tau = 7 \times 10^4$ s the frequency stability obtained is equal to 3.2×10^4 Hz. Thus, to see how the long-term stability impacts on the POP noise, the contribution to the clock frequency stability due to laser frequency fluctuations is estimated to be $\delta_y(7 \times 10^4) = 3.2 \times 10^4 \cdot \frac{\Delta y}{\Delta \nu_L} = 10^{-15}$. The second one has at $\tau = 7 \times 10^4$ s a frequency stability equal to 1.1×10^5 Hz with a corresponding clock frequency stability of 3.3×10^{-15} . The two measurements are similar within a factor 2. The discrepancy is probably due to more or less quite environmental conditions in the two cases.

In conclusion, thanks to the collaboration with Leonardo S.p.A. company there was the opportunity to use one of their lasers.

The laser diode, SN GI-00259, made by Eagleyard with a butterfly package is used. It is locked on the $F = 1 \rightarrow F' = 1,2$ transition as reported in figure 1.4, and it operates with a setpoint of 80 mA at 25.8 °C.

The same stabilization scheme used for the other laser diodes is employed but with the addition of a second probe, which can be used or not. And also with an attenuator that can reduce the power of the signal.

The beatnote between Leonardo laser diode and the INRIM one is obtained replacing the fiber laser with the Leonardo laser diode as input of the optical setup. The frequency of the beatnote is obtained equal to 80 MHz in the case of both lasers locked on different sub-Doppler peaks.

The relative stability for medium-long terms of the two coupling systems is evaluated by measuring the frequency of beatnote over time and the frequency with the same acquisition setup as in the previous stability measurements, to see how the long-term stability impacts the POP noise, as reported in figure 5.3.

Using the experimental POP clock sensitivity in eq.(5.3), the measurements are listed in the table 5.3.

Clock frequency stability at $\tau = 7 \times 10^4$ s	
DFB SN FB-04036	10^{-15}
DFB SN FB-04038	3.3×10^{-15}
LEONARDO DFB	10^{-15}

Table 5.3: POP clock frequency stability.

The frequency stability measurement of the Leonardo laser diode respect the INRIM one, is lower than the first setup used, probably due to the greater stability. A slightly better short-term stability is observable with the new setup, as reported in figure 5.3, probably due to a different stabilization parameters. But, the curve presents the starting of a bump at long time of measurement due to the laboratory

temperature changing, so probably gives a systematic change.

The laser contribution (blue curve in figure 5.4) is compared with the best reported POP laboratory prototype (black curve in figure 5.4 [7]) and with next-generation Galileo specification. The right scale in figure 5.4 shows that the frequency instability of the diode laser induces a contribution to the clock instability below 10^{-14} at all averaging times. The laser frequency stability is measured to be 3 kHz at 10^3 s (left scale), which corresponds to a frequency instability contribution of 10^{-16} (right scale) for the POP clock. This result shows that the laser frequency does not limit the current laboratory prototype and it is compliant with the target specification of the next-generation clocks of the Galileo project [9].

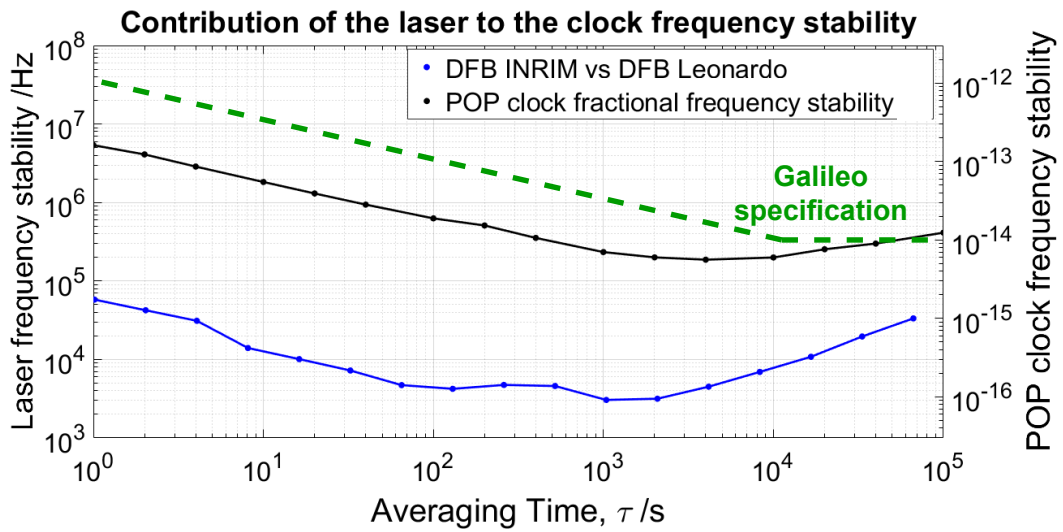


Figure 5.4: Contribution of the laser to the POP clock frequency stability.

Chapter 6

Conclusions

In this thesis the DFB laser was characterized in terms of frequency noise and stability. The power spectral density was measured with a beatnote setup and was the first step to have a complete understanding of Rb clock noise sources. The laser frequency noise was measured with different conditions. The first one was the laser diode change, which had almost the same behavior with a small difference at high frequencies. Then, the current driver contribution was analyzed, to understand that the characteristics of the laser diodes were limited by the current driver, that it is dominant particularly above 500 Hz.

After, the laser diode intrinsic noise in all the condition was computed. It is almost flicker of frequency for two decades, from 10 Hz to 1 kHz.

The frequency noise impacts on the short term, and on medium-long term are analyzed. The stability of many environmental parameters was started to play a particularly role for averaging times above 1000 s. Then, the relative stability for medium-long terms of the two coupling systems is evaluated by measuring the frequency of beatnote and the frequency with the same acquisition setup. The laser frequency long-term stability and the impact on the POP clock were reported, to understand the laser behavior. The frequency stability measurement of the Leonardo laser diode respect the INRIM one, was lower than the first setup used, probably due to the greater stability. A better short-term stability was observed by using Leonardo's laser.

The frequency stability contribution was negligible compared to other instability sources (temperature, laser intensity and so on) for the current POP prototype. The frequency instability results obtained were compliant with the target specifications for the next generation clocks of the Galileo project.

Possible upgrades of the experimental setup will be the use of lower frequency noise current driver. The latter should be acquired in the case of new resources, to explore the spectral purity of diodes. Also, it will be possible to improve the

existing driver circuit to remove the bumps and use the drivers analyzed before. Also, if the frequency analysis would be enlarged to more inputs using different laser diodes, can be done the cross-correlation among them. After the building of the cross-correlation working table, an absolute characterization of noise and stability can be obtained in order to understand the real noise of the lasers analyzed. In fact, in the thesis, the fiber laser is considered as a reference in the first setup, with the INRIM DFB and the fiber laser. But, with this improvement and the availability of more lasers became possible to analyze its noise floor and stability behavior in comparison with other references.

One last improvement of the POP could be the treatment of short-term stability. Indeed, a theoretical model is under development to estimate the short-term stability contribution starting from the frequency noise spectrum. The experimental setup that has been characterized in the thesis will be useful for testing the theory of the frequency noise transfer.

Bibliography

- [1] Ryan T. Dupuis, Thomas J. Lynch, and John R. Vaccaro. «Rubidium Frequency Standard for the GPS IIF program and modifications for the RAFS-MOD Program». In: (2008), pp. 655–660. DOI: 10.1109/FREQ.2008.4623081 (cit. on p. 1).
- [2] M. Bloch, D. Leonard, O. Mancini, and T. McClelland. «Emerging applications requiring precision time and frequency». In: (2009), pp. 364–371. DOI: 10.1109/FREQ.2009.5168202 (cit. on p. 1).
- [3] Pierre Waller, Francisco Gonzalez, Stefano Binda, Ilaria Sesia, Irene Hidalgo, Guillermo Tobias, and Patrizia Tavella. «The In-Orbit performances of GIOVE clocks». In: *IEEE Transactions on Ultrasonics, Ferroelectrics, and Frequency Control* 57.3 (2010), pp. 738–745. DOI: 10.1109/TUFFC.2010.1472 (cit. on p. 1).
- [4] S. Revniviykh. «GLONASS status and modernization». In: *International GNSS Committee IGC-7 Beijing* (2012), pp. 4–9. URL: <http://www.unoosa.org/pdf/icg/2012/icg-7/3-1.pdf> (cit. on p. 1).
- [5] A. Godone, Filippo Levi, C.E. Calosso, and Salvatore Micalizio. «High-performing vapor-cell frequency standards». In: *Rivista del Nuovo Cimento* 38 (Mar. 2015), pp. 133–171. DOI: 10.1393/ncr/i2015-10110-4 (cit. on pp. 1, 3, 4, 6).
- [6] Jacques Haesler et al. «Low-power and low-profile miniature atomic clock ceramic based flat form factor miniature atomic clock physics package (C-MAC)». In: (2017), pp. 55–56. DOI: 10.1109/FCS.2017.8088798 (cit. on p. 1).
- [7] A. Godone S. Micalizio C. E. Calosso and F. Levi. «Metrological characterization of the pulsed Rb clock with optical detection». In: *Metrologia* 49.4 (May 2012), pp. 425–436. DOI: 10.1088/0026-1394/49/4/425. URL: <https://doi.org/10.1088/0026-1394/49/4/425> (cit. on pp. 1, 5–8, 49, 51).

-
- [8] S Micalizio, F Levi, CE Calosso, M Gozzelino, and A Godone. «A pulsed-Laser Rb atomic frequency standard for GNSS applications». In: *GPS Solutions* 25.3 (2021), pp. 1–13 (cit. on pp. 1, 2, 4).
- [9] P. Arpesi et al. «Rubidium Pulsed Optically Pumped Clock for Space Industry». In: (2019), pp. 1–3. DOI: 10.1109/FCS.2019.8856140 (cit. on pp. 1, 51).
- [10] Michele Gozzelino. «Pulsed Rubidium clock towards space applications. Compact design and advanced locking techniques for a vapor-cell microwave frequency standard». Doctoral Thesis. Politecnico di Torino, Mar. 2020 (cit. on pp. 1, 6, 9).
- [11] Claudio Eligio Calosso, Michele Gozzelino, Aldo Godone, Haixiao Lin, Filippo Levi, and Salvatore Micalizio. «Intensity Detection Noise in Pulsed Vapor-Cell Frequency Standards». In: *IEEE Transactions on Ultrasonics, Ferroelectrics, and Frequency Control* 67.5 (2020), pp. 1074–1079. DOI: 10.1109/TUFFC.2019.2957418 (cit. on pp. 1, 3).
- [12] J. C. Camparo. «The rubidium atomic clock and basic research». In: *Phys. Today* 60.11 (Nov. 2007), pp. 33–39. DOI: 10.1063/1.2812121. URL: <https://doi.org/10.1063/1.2812121> (cit. on p. 2).
- [13] James Camparo and Gilda Fathi. «Discharge Lamps for Rb Atomic Clocks: The Role of rf-Power». In: *2009 IEEE International Frequency Control Symposium Joint with the 22nd European Frequency and Time Forum* (May 2009), pp. 994–997. DOI: 10.1109/FREQ.2009.5168340 (cit. on p. 2).
- [14] W. J. Riley. «A History of the Rubidium Frequency Standard». In: *IEEE UFFC-S History* (Dec. 2019). URL: <http://ieee-uffc.org/about-%20us/history/a-history-of-the-rubidium-frequency-standard.pdf> (cit. on p. 2).
- [15] S. Pancharatnam. «Light Shifts in Semiclassical Dispersion Theory». In: *J. Opt. Soc. Am.* 56.11 (Nov. 1966), pp. 1636–1636. DOI: 10.1364/JOSA.56.001636. URL: <http://www.osapublishing.org/abstract.cfm?URI=josa-56-11-1636> (cit. on p. 2).
- [16] V Formichella, J Camparo, and Patrizia Tavella. «Influence of the ac-Stark shift on GPS atomic clock timekeeping». In: *Applied Physics Letters* 110.4 (2017), p. 043506 (cit. on p. 2).
- [17] Etienne Batori, Nil Almat, Christoph Affolderbach, and Gaetano Mileti. «GNSS-grade space atomic frequency standards: Current status and ongoing developments». In: *Advances in Space Research* (2020). ISSN: 0273-1177. DOI: <https://doi.org/10.1016/j.asr.2020.09.012>. URL: <https://www.sciencedirect.com/science/article/pii/S0273117720306414> (cit. on p. 3).

- [18] Bird M.K. «The Huygens Doppler Wind Experiment». In: *Russell C.T. (eds) The Cassini-Huygens Mission. Springer, Dordrecht.* (2003). DOI: https://doi.org/10.1007/978-94-017-3251-2_16 (cit. on p. 3).
- [19] R. P. FRUEHOLZ and M. WUN-FOGLE. «Finite Difference Numerical Analysis of Phase-Boundary Reaction Models for Cesium Penetration Into Glass». In: *Journal of the American Ceramic Society* 66.9 (1983), pp. 605–610. DOI: <https://doi.org/10.1111/j.1151-2916.1983.tb10606.x> (cit. on p. 3).
- [20] M Gharavipour, C Affolderbach, S Kang, T Bandi, F Gruet, M Pellaton, and G Mileti. «High performance vapour-cell frequency standards». In: *Journal of Physics: Conference Series* 723 (June 2016), p. 012006. DOI: 10.1088/1742-6596/723/1/012006 (cit. on p. 3).
- [21] Wolfgang Demtröder. *Laser spectroscopy: basic concepts and instrumentation.* Springer Science & Business Media, 2013 (cit. on p. 3).
- [22] Thejesh Bandi, Christoph Affolderbach, Camillo Stefanucci, Francesco Merli, Anja K. Skrivervik, and Gaetano Mileti. «Compact high-performance continuous-wave double-resonance rubidium standard with $1.4 \times 10^{-13} \tau^{-1/2}$ stability». In: *IEEE Transactions on Ultrasonics, Ferroelectrics, and Frequency Control* 61.11 (2014), pp. 1769–1778. DOI: 10.1109/TUFFC.2013.005955 (cit. on p. 3).
- [23] Mandache C. Vanier J. «The passive optically pumped Rb frequency standard: the laser approach». In: *Applied Physics B* 87 (June 2007), pp. 565–593. DOI: 10.1007/s00340-007-2643-5 (cit. on p. 4).
- [24] N. Cyr, M. Tetu, and M. Breton. «All-optical microwave frequency standard: a proposal». In: *IEEE Transactions on Instrumentation and Measurement* 42.2 (1993), pp. 640–649. DOI: 10.1109/19.278645 (cit. on p. 4).
- [25] Vanier J. «Atomic clocks based on coherent population trapping: a review». In: *Applied Physics B* 81 (Aug. 2005), pp. 421–442. DOI: 10.1007/s00340-005-1905-3 (cit. on p. 4).
- [26] Bonnie L Schmittberger Marlow and David R Scherer. «A Review of Commercial and Emerging Atomic Frequency Standards». In: *IEEE Transactions on Ultrasonics, Ferroelectrics, and Frequency Control* (2021) (cit. on p. 4).
- [27] John Kitching. «Chip-scale atomic devices». In: *Applied Physics Reviews* 5.3 (2018), p. 031302 (cit. on p. 4).
- [28] A. Brannon, M. Jankovic, J. Breitbarth, Z. Popovic, V. Gerginov, V. Shah, S. Knappe, L. Hollberg, and J. Kitching. «A Local Oscillator for Chip-Scale Atomic Clocks at NIST». In: (2006), pp. 443–447. DOI: 10.1109/FREQ.2006.275426 (cit. on p. 4).

- [29] Enric Fernández, David Calero, and M. Eulàlia Parés. «CSAC Characterization and Its Impact on GNSS Clock Augmentation Performance». In: *Sensors* 17.2 (2017). DOI: 10.3390/s17020370 (cit. on p. 4).
- [30] John Kitching, Svenja Knappe, and Leo Hollberg. «Miniature vapor-cell atomic-frequency references». In: *Applied physics letters* 81.3 (2002), pp. 553–555 (cit. on p. 4).
- [31] Norman F. Ramsey. «A Molecular Beam Resonance Method with Separated Oscillating Fields». In: *Phys. Rev.* 78 (June 1950), pp. 695–699. DOI: 10.1103/PhysRev.78.695 (cit. on p. 5).
- [32] Salvatore Micalizio, Aldo Godone, Filippo Levi, and Claudio Calosso. «Pulsed optically pumped ^{87}Rb vapor cell frequency standard: A multilevel approach». In: *Phys. Rev. A* 79 (1 Jan. 2009), p. 013403. DOI: 10.1103/PhysRevA.79.013403 (cit. on p. 5).
- [33] Christoph Affolderbach, C Andreeva, S Cartaleva, T Karaulanov, Gaetano Mileti, and D Slavov. «Light-shift suppression in laser optically pumped vapour-cell atomic frequency standards». In: *Applied Physics B* 80.7 (2005), pp. 841–848 (cit. on p. 6).
- [34] Aldo Godone, Filippo Levi, Salvatore Micalizio, and Claudio Calosso. «Coherent-population-trapping maser: Noise spectrum and frequency stability». In: *Phys. Rev. A* 70 (1 July 2004), p. 012508. DOI: 10.1103/PhysRevA.70.012508 (cit. on p. 6).
- [35] Claudio E. Calosso, Aldo Godone, Filippo Levi, and Salvatore Micalizio. «Enhanced temperature sensitivity in vapor-cell frequency standards». In: *IEEE Transactions on Ultrasonics, Ferroelectrics, and Frequency Control* 59.12 (2012), pp. 2646–2654. DOI: 10.1109/TUFFC.2012.2505 (cit. on p. 7).
- [36] William J Riley. «The physics of the environmental sensitivity of rubidium gas cell atomic frequency standards». In: *IEEE transactions on ultrasonics, ferroelectrics, and frequency control* 39.2 (1992), pp. 232–240 (cit. on p. 8).
- [37] William Moreno, Matthieu Pellaton, Christoph Affolderbach, and Gaetano Mileti. «Barometric effect in vapor-cell atomic clocks». In: *IEEE transactions on ultrasonics, ferroelectrics, and frequency control* 65.8 (2018), pp. 1500–1503 (cit. on p. 8).
- [38] B François, CE Calosso, M Abdel Hafiz, Salvatore Micalizio, and R Boudot. «Simple-design ultra-low phase noise microwave frequency synthesizers for high-performing Cs and Rb vapor-cell atomic clocks». In: *Review of Scientific Instruments* 86.9 (2015), p. 094707 (cit. on p. 8).

-
- [39] E. Rubiola. *Phase Noise and Frequency Stability in Oscillators*. The Cambridge RF and Microwave Engineering Series. June 2010. Chap. 1 (cit. on pp. 10, 11, 47).
- [40] Enrico Rubiola. «Enrico’s Chart of Phase Noise and Two-Sample Variances». In: *European Frequency and Time Seminar* (Sept. 2019) (cit. on pp. 13, 14).
- [41] E. Rubiola. *Almost All About Phase Noise*. Mar. 2021. Chap. 2 (cit. on p. 13).
- [42] E. Rubiola. *The measurement of AM noise of oscillators*. Dec. 2005 (cit. on p. 13).
- [43] Claudio E. Calosso, Cecilia Clivati, and Salvatore Micalizio. «Avoiding Aliasing in Allan Variance: An Application to Fiber Link Data Analysis». In: *IEEE Transactions on Ultrasonics, Ferroelectrics, and Frequency Control* 63.4 (2016), pp. 646–655. DOI: 10.1109/TUFFC.2016.2519265 (cit. on p. 13).
- [44] Larry A Coldren, Scott W Corzine, and Milan L Mashanovitch. *Diode lasers and photonic integrated circuits*. Vol. 218. John Wiley & Sons, 2012 (cit. on pp. 14, 15).
- [45] C. Henry. «Theory of the linewidth of semiconductor lasers». In: *IEEE Journal of Quantum Electronics* 18.2 (1982), pp. 259–264. DOI: 10.1109/JQE.1982.1071522 (cit. on p. 15).
- [46] TH Maiman. «Optical and microwave-optical experiments in ruby». In: *Physical review letters* 4.11 (1960), p. 564 (cit. on p. 15).
- [47] AD White and JD Rigden. «Continuous gas maser operation in visible». In: *Proceedings of the Institute of Radio Engineers* 50.7 (1962), p. 1697 (cit. on p. 15).
- [48] R. Braunstein. «Radiative Transitions in Semiconductors». In: *Phys. Rev.* 99 (6 Sept. 1955), pp. 1892–1893. DOI: 10.1103/PhysRev.99.1892 (cit. on p. 15).
- [49] Anthony E Siegman. «New developments in laser resonators». In: 1224 (1990), pp. 2–14 (cit. on p. 15).
- [50] Christoph Affolderbach and Gaetano Mileti. «A compact laser head with high-frequency stability for Rb atomic clocks and optical instrumentation». In: *Review of Scientific Instruments* 76.7 (2005), p. 073108. DOI: 10.1063/1.1979493 (cit. on p. 15).
- [51] R. Burnham, D. Scifres, and W. Streifer. «Single-heterostructure distributed-feedback GaAs-diode lasers». In: *IEEE Journal of Quantum Electronics* 11.7 (1975), pp. 439–449. DOI: 10.1109/JQE.1975.1068649 (cit. on p. 16).
- [52] Orazio Svelto. *Solid-State, Dye, and Semiconductor Lasers*. Boston, MA: Springer US, 2010, pp. 375–430. DOI: 10.1007/978-1-4419-1302-9_9 (cit. on p. 16).

- [53] Jeff Hecht. «Short history of laser development». In: *Optical Engineering* 49.9 (2010), pp. 1–23. DOI: 10.1117/1.3483597 (cit. on p. 16).
- [54] Michalis N Zervas and Christophe A Codemard. «High power fiber lasers: a review». In: *IEEE Journal of selected topics in Quantum Electronics* 20.5 (2014), pp. 219–241 (cit. on p. 17).
- [55] «The effective absorption coefficient in double-clad fibres». In: *Optics Communications* 99.5 (1993), pp. 331–335. DOI: [https://doi.org/10.1016/0030-4018\(93\)90338-6](https://doi.org/10.1016/0030-4018(93)90338-6) (cit. on p. 17).
- [56] Frank J Duarte. *Tunable laser applications*. Vol. 150. CRC press, 2008 (cit. on p. 17).
- [57] Nil Almat, William Moreno, Matthieu Pellaton, Florian Gruet, Christoph Affolderbach, and Gaetano Mileti. «Characterization of Frequency-Doubled 1.5 μ m Lasers for High-Performance Rb Clocks». In: *IEEE transactions on ultrasonics, ferroelectrics, and frequency control* 65.6 (2018), pp. 919–926 (cit. on pp. 17, 22).
- [58] Olivier Llopis, Pierre-Henri Merrer, Houda Brahim, Khaldoun Saleh, and Pierre Lacroix. «Phase noise measurement of a narrow linewidth CW laser using delay line approaches». In: *Optics letters* 36.14 (2011), pp. 2713–2715 (cit. on p. 18).
- [59] Hanne Ludvigsen and Erik Bødtker. «New method for self-homodyne laser linewidth measurements with a short delay fiber». In: *Optics communications* 110.5-6 (1994), pp. 595–598 (cit. on p. 18).
- [60] Peter Horak and Wei H Loh. «On the delayed self-heterodyne interferometric technique for determining the linewidth of fiber lasers». In: *Optics express* 14.9 (2006), pp. 3923–3928 (cit. on p. 18).
- [61] Wendell D. Seal, Algie L. Lance and Frederik Labaar. «Phase Noise and AM Noise Measurements in the Frequency Domain, TN190». In: *Infrared and Millimeter Waves* 11 (1984), pp. 239–289 (cit. on p. 18).
- [62] R. Paschotta. «article on 'beat note'». In: *Encyclopedia of Laser Physics and Technology, Wiley-VCH* (Oct. 2008). URL: https://www.rp-photonics.com/beat_note.html (cit. on p. 18).
- [63] K. Razdan and D.A. Van Baak. «Demonstrating optical beat notes through heterodyne experiments». In: *American Journal of Physics* 70.10 (2002), pp. 1061–1067. DOI: 10.1119/1.1484150 (cit. on p. 19).
- [64] NKT Photonics. *Bootstik HPA Users Manual*. Sept. 2016 (cit. on p. 21).

- [65] Dan Cohen, Igal Tiroshi, and Shmuel Eylon. «High-Speed Frequency-to-Voltage Converter with 0.01-Percent Accuracy». In: *IEEE Transactions on Instrumentation and Measurement* 22.2 (1973), pp. 108–113. DOI: 10.1109/TIM.1973.4314119 (cit. on p. 29).
- [66] Agilent Technologies. *Datasheet Agilent E8257D PSG, Microwave Analog Signal Generator*. Aug. 2009 (cit. on p. 32).
- [67] Daniel A. Steck. «Rubidium 87 D Line Data». In: *Oregon Center for Optics and Department of Physics, University of Oregon* (July 2021). URL: <http://steck.us/alkalidata> (cit. on p. 40).
- [68] Salvatore Micalizio, Aldo Godone, Filippo Levi, and Claudio Calosso. «Medium-long term frequency stability of pulsed vapor cell clocks». In: *IEEE Transactions on Ultrasonics, Ferroelectrics, and Frequency Control* 57.7 (2010), pp. 1524–1534. DOI: 10.1109/TUFFC.2010.1583 (cit. on p. 49).